

1 **Switching Extensional and Contractional Tectonics in the**
2 **West Kunlun Mountains During Jurassic: Responses to the**
3 **Neo-Tethyan Geodynamics along the Eurasian Margin**

4
5 Hong-Xiang Wu^{1,2}, Han-Lin Chen^{1,2*}, Andrew V. Zuza³, Yildirim Dilek⁴, Du-Wei
6 Qiu^{1,2}, Qi-Ye Lu^{1,2}, Feng-Qi Zhang^{1,2}, Xiao-Gan Cheng^{1,2}, Xiu-Bin Lin^{1,2}

7
8 1 School of Earth Sciences, Zhejiang University, Hangzhou, China.

9 2 Structural Research Center of Oil & Gas Bearing Basin of Ministry of
10 Education, Hangzhou, China.

11 3 Nevada Bureau of Mines and Geology, Nevada Geosciences, University of
12 Nevada, Reno, NV, USA.

13 4 Department of Geology & Environmental Earth Science, Miami University,
14 Oxford, OH, USA.

15
16 ORCID: 0000-0003-4997-8715 (Hong-Xiang Wu)

17
18 *Corresponding author: hlchen@zju.edu.cn (Han-Lin Chen)

19
20 Address: No. 1 Hainayuan Building, Zijingang Campus, Zhejiang University,
21 866 Yuhangtang Road, Hangzhou, Zhejiang, P.R.China.

22
23 Submitted to: Solid Earth

24 **Abstract:** The Tethyan Orogenic Belt records a long-lived geological cycle
25 involving subduction and collision along the southern margin of the Eurasian
26 continent. The West Kunlun Mountains, located at the junction between the
27 Tibetan and Pamir orogens within the Tethyan realm, records multiple orogenic
28 events from the Paleozoic to the Cenozoic that shape the northwestern Tibetan
29 Plateau. However, deciphering the complex Mesozoic contractional and
30 extensional tectonics to interpret the broader Tethyan geodynamics remains
31 challenging. To address the tectonic transition following the early Cimmerian
32 (Late Triassic) collision, this study investigates the newly identified Jurassic
33 sedimentary strata and volcanic rocks in the West Kunlun Mountains. Zircon
34 geochronological results of basalts and sandstones reveal that this ~ 2.5-km-
35 thick package was deposited at ca. 178 Ma, rather than the previously reported
36 Neoproterozoic age. The alkaline basalts at the top of the formation exhibit
37 chemical compositions similar to oceanic island basalts, consistent with the
38 intracontinental extension environment revealed by the upward-fining
39 sedimentary pattern. Provenance analysis, including conglomerate clast
40 lithologies and detrital zircons, suggests a substantial contribution from
41 adjacent basement sources, likely influenced by the normal faulting during initial
42 rift stage. These findings indicate that the West Kunlun Mountains rapidly
43 transitioned into an extensional setting after suturing with Cimmerian terranes.
44 The regional structure, stratigraphy and magmatism suggest that the Early-
45 Middle Jurassic southwestern Tarim basin was subsequently inverted during
46 the Late Jurassic and earliest Cretaceous. We propose that the Mesozoic
47 deformational history in the West Kunlun Mountains was related to the
48 northward subduction of the Neo-Tethys Ocean, as it transitioned from

49 southward retreat to northward flat-slab advancement. Comparing with the
50 entire strike-length of the Eurasian Tethyan orogen, we find that the subduction
51 mode varied from the west to the east, reflecting the broad geodynamic
52 changes to, or initial conditions of, the Neo-Tethyan system.

53

54 **Keywords:** Tethyan Orogenic Belt; West Kunlun Mountains; Jurassic basalts;
55 Basin evolution; Subduction retreating and advancing.

56

57 **1 Introduction**

58 The Tethyan Orogenic Belt is an over 15,000 km trans-Eurasian orogenic
59 system with a series of mountain chains and orogenic plateaus. (Fig. 1a;
60 Şengör, 1987; Metcalfe, 2013; Wu et al., 2020). The evolution of the Tethyan
61 Orogenic Belt involved multiple phases of ocean basin opening and closure (i.e.,
62 the Proto-, Paleo-, and Neo-Tethys oceans) throughout the Phanerozoic era,
63 which resulted in the development of multiple orogenic belts across the
64 Eurasian continent (Stampfli, 2000; Wan et al., 2019; Metcalfe, 2021). The
65 complex history of accretionary and collisional orogenesis in the Tethyan realm
66 is intricately linked to the breakup and formation of two mega-landmasses,
67 Gondwana and Laurasia (Şengör et al, 1988; Stampfli and Borel, 2002; Zuza
68 and Yin, 2017; Li et al., 2018; Wang et al., 2018). Documenting the mode and
69 nature of the accretionary and collisional events in the Mesozoic history of the
70 Tethyan orogenic system is, therefore, important for understanding the
71 continental dynamics of Eurasia.

72 The Mesozoic Tethyan Orogenic Belt involved orogenesis, rifting, and
73 basin evolution, associated with the convergence between the southern Asian
74 margin and Cimmerian terranes derived from Gondwana (e.g., Kazmin, 1991;
75 Stampfli and Borel, 2002; Angiolini et al., 2013; Robinson, 2015). The Mesozoic
76 tectonic evolution of the Tethyan realm exhibits significant variations from the
77 west to the east (Şengör, 1984; Zhu et al., 2022). In the Western Asian section
78 of the Tethyan Orogenic Belt, geochronological and geochemical data from
79 different magmatic rock assemblages suggest a northwestward-propagating
80 continental rift system along the southern margin of the Central Iran Block
81 during the Early Jurassic to Early Cretaceous (Hunziker et al., 2015; Lechmann

82 et al., 2018; Azizi and Stern, 2019). This process is envisioned to have been
83 associated with subduction geodynamics involving multiple intraoceanic
84 subduction zones, slab tearing, and alternating slab rollback and advance
85 within Neo-Tethys (Zhang et al., 2018; Jafari et al., 2023). Conversely, in the
86 Eastern Asian section of the Tethyan Orogenic Belt (i.e. Tibetan sector), an
87 Andean-type orogeny along the southern margin of Eurasia from the Early
88 Jurassic to the Early Cretaceous has been proposed to explain deformation and
89 sedimentation patterns in the southern Tibetan Plateau (Kapp et al., 2007;
90 Zhang et al., 2012; Xie and Dilek, 2023). This process was punctuated by
91 Toarcian-Aalenian back-arc rifting event resulting from retreat of the subducting
92 Neo-Tethyan seafloor (Hou et al., 2015; Wei et al., 2017).

93 The West Kunlun Mountains, stretching from the northern Pamir to
94 northwestern Tibetan Plateau, occupy a critical position at the junction between
95 the western and eastern Tethyan Orogenic Belts (Fig. 1b; Şengör, 1984; Wu et
96 al., 2016). The West Kunlun Mountains involved the closure of the Paleo-
97 Tethyan Ocean in the Triassic-Jurassic, followed by Cenozoic deformation and
98 uplift during the Himalayan orogeny (Mattern and Schneider, 2000; Cao et al.,
99 2015; Li et al., 2019; Xiao et al., 2002). Hence, the Mesozoic geology of the
100 West Kunlun Mountains documents the plate tectonic history of the junction
101 region within the Tethyan realm, providing pivotal insights into the formation of
102 this extensive orogenic system. In particular, the Cimmerian Orogeny in the
103 West Kunlun region critically records the collision between the Gondwana-
104 derived continental fragments and the southern Eurasian margin in the latest
105 Triassic to late Jurassic (e.g., Şengör, 1979), but the timing and duration of this
106 orogen remains equivocal. Existing interpretations of the Jurassic

107 palaeogeography and evolution vary, ranging from syn-orogenic (Cao et al.,
108 2015), post-orogenic (Wu et al., 2021), to transtensional (Sobel, 1999),
109 because of the scarcity of the relevant geological record from this period.
110 Significant challenges also persist in understanding the Mesozoic evolution of
111 the Pamir terranes (Angiolini et al., 2013), including the timing of suturing and
112 exact kinematics of related deformation (Robinson, 2015). The Cenozoic
113 contractional deformation episodes, due the northward subduction of the Neo-
114 Tethyan Ocean and the collision of India with Eurasia, further complicates our
115 understanding in this remote region (Burtman and Molnar, 1993; Cowgill, 2010).
116 The limited knowledge of the Jurassic and Cretaceous evolution of the Pamir
117 interior has been preliminarily deduced from the timing and nature of regional
118 magmatic activities (Chapman et al., 2018) that are challenged by the
119 information derived from the surrounding, fragmented sedimentary basins
120 (Leith, 1985; Wu et al., 2021).

121 To better understand the regional evolution and tectono-magmatic
122 processes in the West Kunlun Mountains, we have undertaken a systematic
123 geochronological and geochemical study and detailed analyses of sedimentary
124 provenance of volcanoclastic rock suites in the Jurassic Kyzyltau-Kandilik basin.
125 By integrating these new results with existing data from the adjacent region,
126 this study provides further constraints on the Mesozoic tectonic history of the
127 central junction of the Tethyan Orogenic Belt and probes the preceding
128 processes that cause the formation of the broad plateau in central Asia.

129

130 **2 Geological framework and sampling**

131 **2.1 Tethyan history**

132 The Tethyan Orogenic Belt separates the main Eurasian cratons and stable
133 platforms in the north from Gondwana - derived continental terranes in the
134 south (e.g., Şengör et al, 1988; Stampfli et al., 1991). The development of the
135 Tethyan Orogenic Belt involves the evolution of multiple ocean basins and their
136 seaways, including the Proto-Tethys, Paleo-Tethys, and Neo-Tethys (Stampfli,
137 2000; Metcalfe, 2021). These ancient ocean basins overlapped in time but
138 closed successively as the Gondwana - derived ribbon continents (i.e., Apulia,
139 Pelagonia, Sakarya, Tauride, South Qiangtang and North Qiangtang and Lhasa)
140 accreted to the southern margin of Eurasia, creating several sub-parallel suture
141 zones stretching from the circum-Mediterranean region, Caucasus, Iranian
142 Plateau, and continuing eastward into the Tibetan Plateau and Southeast Asia
143 (Fig. 1a; Dilek and Moores, 1990; Wu et al., 2020; Metcalfe, 2021).

144 The Cenozoic indentation of the Pamirs fundamentally affected the
145 deformation pattern of the Tethyan Orogenic Belt and geographically divided
146 the belt into western and eastern sectors (Tapponnier et al., 1981). The history
147 of the Proto-Tethys was linked to the breakup of the Rodinia supercontinent
148 (Zhao et al., 2018). The western segment of the Proto-Tethys has been defined
149 as a Cambrian-Silurian ocean existing between Baltica and Gondwana,
150 whereas the eastern Proto-Tethys appears to have been closed earlier in the
151 Early Silurian, as a series of Asian blocks collided onto the northern margin of
152 Gondwana (e.g., Stampfli and Borel, 2002). The opening of the Paleo- and Neo-
153 Tethyan ocean basins was related to slab pull forces that caused the
154 detachment of the Hun (including the Tarim, North and South China) and
155 Cimmerian terrane ribbons from the northern margin of Gondwanaland,
156 respectively (Stampfli and Borel, 2002; Ruban et al., 2007). These terranes

157 were successively transferred northward to the Eurasian continent, causing the
158 closure of these internal seaways during the Cimmerian and Himalayan
159 orogenies at the end of the Triassic and the beginning of the Cenozoic,
160 respectively (Dilek and Furnes, 2019; Wan et al., 2019).

161 The final demise of the Paleo-Tethyan Ocean and the initiation of
162 subduction in the Neo-Tethyan Ocean occurred simultaneously in the Triassic -
163 earliest Jurassic, which is of vital importance for comprehension of the cyclical
164 Tethyan evolution (Wan et al., 2019). The West Kunlun Mountains, situated to
165 the north of the Pamir syntaxis, forms the western extent of the Tibetan Plateau
166 (Fig. 1b-c). They constitute an important spatial link between the western and
167 eastern domains of the Tethyan Orogenic Belt. The formation of the West and
168 East Kunlun Mountains, involved accretionary and collisional orogeneses
169 during the closure of the Proto-Tethys and Paleo-Tethys oceans (Mattern and
170 Schneider, 2000; Xiao et al., 2005; Dong et al., 2018). The East Kunlun
171 Mountains are displaced to the north relative to the West Kunlun Mountains by
172 the dextral Altyn-Tagh strike-slip fault (Fig. 1b). During the Early Paleozoic, the
173 closure of the Proto-Tethys Ocean led to the collision of the Tarim Craton (North
174 Kunlun) and the South Kunlun terrane along the Kudi suture zone (Fig. 1c;
175 Zhang et al., 2019a). After splitting from eastern Gondwana in the Devonian -
176 Carboniferous, the Tianshuihai - Qiangtang blocks travelled northward towards
177 the Tarim Craton because of the subduction of the Paleo-Tethyan Ocean. These
178 blocks ultimately collided with the Tarim Craton at the latest Triassic, forming
179 the Mazar - Kangxiwa suture zone (Fig. 1c; Xiao et al., 2005; Metcalfe, 2021).
180 The Pamir terranes (including the Central Pamir, South Pamir, and Karakoram),
181 commonly regarded as the western counterpart of the Qiangtang block, rifted

182 from Gondwana during the Permian (Robinson, 2015; Angiolini et al., 2015).
183 The major Cimmerian orogenic unconformity between the Lower Jurassic and
184 the deformed Upper Triassic strata is generally considered to mark the timing
185 of the amalgamation of these Pamir terranes onto the Eurasian margin
186 (Angiolini et al., 2013; Li et al., 2022b).

187 The mid-Mesozoic tectonic evolution of the West Kunlun Mountains and
188 Pamir is somewhat enigmatic, as the first-order geodynamic mechanisms for
189 widespread deformation remain unclear. Several major exhumation events,
190 including the Late Triassic and Early Jurassic, Middle-Late Jurassic, Early
191 Cretaceous, and Late Cretaceous, are documented by low-temperature
192 thermochronology in the mountain ranges and surrounding basins (Sobel, 2013;
193 Cao et al., 2015; Li et al., 2019, 2023). Mid-Cretaceous granitoids are
194 widespread in the South Pamir and Karakoram. A Jurassic to Cretaceous
195 polymetamorphic history is also displayed by monazite ages (Faisal et al.,
196 2014). The basement cooling as well as magmatic, and metamorphic activities
197 have previously been interpreted as associated with far-field stress effects of
198 collisional events (Yang et al., 2017) or retro-arc contraction during an Andean-
199 type subduction of the Neo-Tethyan Ocean (Chapman et al., 2018). These
200 Mesozoic structures within the orogenic belts were intensely reworked by the
201 Cenozoic deformation during the Himalayan orogeny (Burtman and Molnar,
202 1993).

203

204 **2.2 Regional geology and sampling strategy**

205 This study focused on the central and southern parts of the northwest-
206 trending Jurassic basin within the West Kunlun Mountains (Fig. 1c). The

207 Kyzyltau region, situated in the central part of this Jurassic basin, preserves
208 thick Early-Middle Jurassic strata. It mainly comprises the Lower Jurassic
209 Shalitashi and Kangsu formations, and the Middle Jurassic Yangye and Taerga
210 formations (Fig. 2a). The Shalitashi Formation comprises a massive, thick
211 conglomerate that overlies the deformed Carboniferous and Permian shallow
212 marine clastic rocks and limestones along an angular unconformity (Fig. 3a).
213 The poorly sorted textures and lateral thickness variations in the conglomerate
214 indicate that its clastic material originated from alluvial fans (Sobel, 1999; Fig.
215 3b-e). The Kangsu and Yangye formations form the main part of the Jurassic
216 strata (Fig. 2a), with total stratigraphic thickness exceeding 1800 meters. The
217 Kangsu Formation mainly comprises stacked greywackes interbedded with
218 coal layers. The Yangye Formation consists mainly of interbedded sandstones
219 and shales exhibiting typical Bouma sequences, indicative of turbidite deposits
220 in a deepwater environment (Wu et al., 2021). The Middle Jurassic Taerga
221 Formation is only exposed in the northeastern side of the region and consists
222 of thinly-bedded shales and siltstones. The Lower to Middle Jurassic
223 stratigraphy forms an upward-fining sequence, indicating the expanding and
224 deepening of the basin over time. Structurally, the Jurassic strata exhibit strong
225 deformation, forming a northwest-trending synclinorium (Fig. 2a). The Cenozoic
226 contraction in the region extensively deformed the coal-bearing strata, resulting
227 in the formation of multi-scale folds and thrusts (Fig. 3f and 3g). Regionally, the
228 Early-Middle Jurassic strata are unconformably overlain by the Late Jurassic
229 Kuzigongsu Formation and the Cretaceous Kezilesu Group, which are
230 characterized by oxidation-colored, massive conglomerate and sandstones
231 (Fig. 3h). Synchronous unconformities also exist in the South Qiangtang and

232 Bangong-Nujiang suture zones (Ma et al., 2017, 2018).

233 In the Kandilik region, geological mapping identified a coal-bearing
234 formation, known as the Lower - Middle Jurassic Yarkant Formation, and a
235 massive conglomerate classified as the Upper Jurassic Kuzigongsu Formation
236 (Fig. 2b). These Jurassic strata were strongly deformed and laterally bounded
237 by a mylonitic shear zone to the west and thrust faults to the east. A stratigraphic
238 unit consisting of gray-black mudstone, siltstone, and fine sandstone is exposed
239 to the east of the Yarkant Formation, with a thickness exceeding 3500 meters
240 (Ma et al., 1991). Abundant mafic dykes intruded into the lower part of the strata
241 (Fig. 3i), causing local contact metamorphism. A suite of volcanic strata
242 composed of several basalt layers are juxtaposed with the thick clastic package
243 along a steeply-dipping fault. Several eruptive episodes are identified within this
244 unit based on alternating volcanic horizons, including volcanic breccia (Fig. 3j),
245 amygdaloidal basalts, and massive basalts (Fig. 3k). These volcanic rocks
246 belong to the part of upper member deposited above the thick clastic strata (Ma
247 et al., 1991). Due to the lack of reliable constraints from chronological results,
248 this stratigraphic unit has long been thought as Precambrian in age (Ma et al.,
249 1991). Structurally, the strata were intensely deformed by regional Kashgar-
250 Yecheng transfer faults (Fig. 2) and bedding dips steeply to the northeast (Fig.
251 3l).

252 In the Kandilik region, one basalt sample (AYBL09) was collected near the
253 thrust fault for geochronological dating (Fig. 2b). Six fresh, undeformed basalt
254 samples were also obtained away from faults for geochemical analysis. These
255 basaltic rock samples consist primarily of plagioclase with a fine columnar
256 texture and anhedral Ti-Fe oxides (Fig. 3m). Plagioclase is locally altered into

257 chlorite. Additionally, one quartz-lithic sandstone sample (AYBL13) was
258 collected for detrital zircon age analysis. This sample exhibits poor sorting and
259 is composed mainly of quartz (~ 30%) with angular shapes, feldspar (<10%),
260 and lithic fragments (> 60%) (Fig. 3n). For regional comparison, two sandstone
261 samples were collected from the Kangsu (KZLT1601) and Yangye formations
262 (KZLT1602) in the Kyzyltau region (Fig. 2a). These sandstones show similar
263 textures and compositions to the clastic sample from the Kandilik region (Fig.
264 3o).

265

266 **3 Methodology**

267 One basalt sample (AYBL09) was collected from the Kandilik section (Fig.
268 2b) for zircon U - Pb geochronology and in-situ trace element analysis. Zircon
269 separation and cathodoluminescence (CL) imaging were done at Yuheng Rock
270 & Mineral Technology Service Co., LTD., Langfang, China. Zircons were
271 analyzed for U - Pb geochronology using an Agilent 8900 ICP-QQQ equipped
272 with an ESI New Wave NWR 193UC (Two Vol2) laser ablation system at Beijing
273 Quick-Thermo Science & Technology Co., Ltd, China. Concordia plots were
274 constructed using IsoplotR (Vermeesch, 2018).

275 To analyze the petrogenesis and tectonic setting of magmatism, six fresh
276 basalt rocks were collected from the same section for determining their major
277 and trace element chemistry. Samples were first crushed, and powdered in an
278 agate mill. Elemental analyses were conducted at Wuhan SampleSolution
279 Analytical Technology Co., Ltd. Major-element analyses were performed by X-
280 ray fluorescence spectrometry (ZSXPrimusII), with analytical uncertainties
281 generally better than 1%. Trace-element contents were determined using an

282 Agilent 7700e ICP-MS.

283 To compare the detrital age patterns and sedimentary provenance, we
284 have conducted zircon U-Pb dating on two sandstones (KZLT1601 and KZLT1602)
285 exposed in the Kyzyltau section, and one sandstone (AYBL13) exposed in the
286 Kandilik section (Fig. 2B). Zircons from samples KZLT1601 and KZLT1602 were
287 analyzed for U - Pb geochronology using a ThermoFisher iCAP RQ ICP-MS
288 equipped with a Cetea Analyte HE laser ablation system at School of Earth
289 Sciences, Zhejiang University. Zircons from sample AYBL13 were analyzed for
290 U - Pb geochronology using an Agilent 8900 ICP-QQQ equipped with an ESI
291 New Wave NWR 193UC (Two Vol2) laser ablation system at Beijing Quick-
292 Thermo Science & Technology Co., Ltd. The Common Pb was corrected with
293 the method proposed by (Andersen, 2002). Concordia plots and Kernel Density
294 Estimate (KDE) plots were constructed using IsoplotR (Vermeesch, 2018) and
295 Density Plotter 8.5 (Vermeesch, 2012), respectively.

296 The details of the analytical procedures and the information of the
297 analytical methodologies, as explained above, are presented in Table S1.

298 The data from the conglomerate in the Shalitashi Formation were collected
299 at eight different sections. Analysis of conglomerate clasts was conducted
300 within a designated 1 square meter area. Our focus was on documenting the
301 lithological compositions of the clasts, with at least one hundred gravels
302 randomly counted at each site.

303

304 **4 Analytical Results**

305 **4.1 Morphology and geochronology of zircons from basalt sample**

306 The results of zircon U-Pb dating of the basalt sample are presented in

307 Table S2. Approximately one hundred and seventy zircon grains have been
308 successfully separated from the basalt sample. Zircon crystals are mostly
309 transparent and colorless, displaying varying lengths ranging between 50-200
310 μm with elongation ratios of 1:1-5:1 (Fig. 4). Upon examination of their
311 cathodoluminescence (CL) images, we have sub-categorized these zircons into
312 two groups based on the presence of oscillatory zoning. The grains showing
313 well-defined growth zoning (type 1) are generally sub-euhedral in shape (no.3
314 in Fig. 4), which imply their magmatic origin (Fig. 4; Hoskin and Schaltegger,
315 2003). Another type (type 2) of zircon displays inconspicuous zoning texture
316 (no.4 in Fig. 4) or yields only faintly visible zoning patterns (no.15 in Fig. 4).
317 Morphological analysis of these zircons reveals a range from needle-shaped
318 and elongated crystals (no.13 in Fig. 4) to stubby and equant forms (no.12 in
319 Fig. 4). A common feature of these varying grains is their subrounded external
320 appearance. This may result from moderate resorption either during the
321 evolution of the magma chamber when the magma is oversaturated with
322 respect to zircon or a certain degree of metamorphism (Corfu et al., 2003). In
323 addition to their "polished" shape, these zircons commonly display nebulous or
324 patchy-zoned centers, without distinct core-rim structures (no.11-13 in Fig. 4).

325 We have conducted a total of thirty-six spot analyses on various types of
326 zircons (Fig. 4), resulting in thirty-three analyses with a > 90% concordance
327 (Fig. 5a). The Th/U ratios of all tested zircons range from 0.04 to 1.52 (Fig. 5d).
328 We cannot assert that all of them are primary crystals without modification
329 simply based on the evaluation of Th/U ratios. However, all of these results
330 yielded concordant ages spanning a broad range from the Early Neoproterozoic
331 to the Jurassic. Type 1 zircon grains have Th/U ratios ranging from 0.38 to 1.44,

332 while type 2 zircon grains exhibit a wider range. Based on the classification and
333 statistical analysis of zircon characteristics, we found that type 1 zircons, which
334 commonly exhibit clear oscillatory zoning, have older $^{206}\text{Pb}/^{238}\text{U}$ ages ranging
335 from 405 Ma to 911 Ma, whereas type 2 zircons display uniform ages between
336 168 Ma and 193 Ma (Table S2). Twenty youngest zircons with the concordant
337 ages define a weighted mean $^{206}\text{Pb}/^{238}\text{U}$ age of 178 ± 2 Ma (MSWD = 0.99) (Fig.
338 5b). We interpret this Toarcian age as the crystallization age of this rock sample.
339 The remaining older zircons yield primarily middle Paleozoic and
340 Neoproterozoic ages, which we interpret as inherited from the country rock.

341

342 **4.2 Whole-rock major and trace elements of basalts**

343 The chemical compositions of the basalt samples from the Kandilik section
344 are provided in Table S4. Except for one sample (AYBL11D), the majority of our
345 samples displays similar geochemical compositions, characterized by low SiO_2
346 (45.7-51.0 wt.%) and MgO (4.78-7.18 wt.%) contents, and Mg\#s ranging
347 between 45 and 52. These samples possess high TiO_2 (2.42-3.34 wt.%) and
348 total alkali ($\text{Na}_2\text{O} + \text{K}_2\text{O} = 5.17\text{-}6.35$ wt.%) contents, and exhibit moderate Al_2O_3
349 contents ranging from 11.1 to 14.4 wt.% and total Fe_2O_3 ranging from 12.6 to
350 13.7 wt.%. In comparison, the sample AYBL11D displays relatively high
351 contents of SiO_2 (55.5 wt.%) and TiO_2 (4.76 wt.%) with a low total alkali content
352 (4.80 wt.%). All basalt samples fall within the alkaline series field as depicted in
353 the total alkali-silica diagram (Fig. 6a). However, it is worth noting that all
354 analyzed samples exhibit varying Loss-on-Ignition ($\text{LOI} = 1.51\text{-}9.81$ wt.%)
355 values, attributed to weathering and alteration effects, with the presence of
356 chlorite and calcite (Fig. 3m). Hence, it is crucial to assess the alteration effects

357 on the chemical compositions of the analyzed samples. The high-field-strength
358 elements (HFSE, such as Nb, Ta, Ti, and Hf) and rare earth elements (REE)
359 are typically immobile during alteration. This is supported by the consistent
360 elemental variations against the most immobile element Zr, as shown in the Fig.
361 S1. Additionally, Cr (25.4–108 ppm) and Ni (27.4–61.2 ppm) in these samples
362 (except AYBL11D) also demonstrate strong correlations with Zr, suggesting that
363 these elements were essentially immobile during alteration. Based on the Nb/Y
364 vs. Zr/TiO₂ diagram proposed by Winchester and Floyd (1977), all samples plot
365 in the alkaline series (Fig. 6b). Therefore, we posit that these rocks are best
366 classified as alkaline basalt.

367 All analyzed samples display consistent chondrite-normalized rare earth
368 element patterns (Fig. 6c), characterized by an enrichment of LREE relative to
369 HREE, with (La/Yb)_N ratios ranging from 6.24 to 7.96. Moreover, their REE
370 patterns exhibit slight negative Eu anomalies ($\delta\text{Eu} = 0.7\text{-}1.0$). The primitive
371 mantle-normalized multi-element diagram illustrates that the analyzed samples
372 are characterized by the enrichment of highly incompatible trace elements
373 relative to low incompatible elements (Fig. 6d). The samples present significant
374 depletion of Sr and slight enrichment in Zr and Hf. No negative Zr-Hf-Ti
375 anomalies are observed in any of the analyzed basalts.

376

377 **4.3 Detrital zircon U–Pb ages from Jurassic sandstones**

378 The zircon U-Pb geochronological dataset for the detrital zircons is
379 presented in Table S2. A total of 101 spot analyses were conducted on zircon
380 grains from sample AYBL13. After filtering grains with greater than 10%
381 discordance, 98 of them met the criteria for inclusion in the Kernel Density

382 Estimate (KDE) visualization (Fig. 7a). The analyzed results reveal that the
383 Th/U ratios of most effective zircons range between 0.12 and 2.61, with only
384 four zircons yielding extremely low values below 0.1 (Fig. 5d). The results
385 suggest that most detrital zircons from sample AYBL13 are of igneous origin
386 (Belousova et al., 2002). The youngest zircon grain from this sandstone yielded
387 an apparent $^{206}\text{Pb}/^{223}\text{U}$ age of 429 ± 5 Ma, whereas the oldest grain has an
388 apparent $^{206}\text{Pb}/^{207}\text{Pb}$ age of 3080 ± 22 Ma. The KDE plot reveals four main age
389 populations with peaks at approximately 446 Ma, 820-955 Ma, 1553 Ma, and
390 2484 Ma (Fig. 7b).

391 For analyzing provenance, two Jurassic samples from Kyzyltau were
392 analyzed for age comparison. The Early Jurassic sample KZLT1601 underwent
393 one hundred spot analyses on randomly selected zircon grains. These
394 measured grains exhibit Th/U ratios ranging from 0.09 to 1.49 (Fig. 5d),
395 consistent with an igneous origin. Eighty-nine zircon ages were plotted on or
396 near the concordant curve (Fig. 7c), providing zircon ages ranging from $369 \pm$
397 6 Ma to 3314 ± 15 Ma. The detrital age spectrum was obtained using the KDE
398 method and revealed similar peaks at approximately 444 Ma, 807 Ma, 1823 Ma,
399 and 2566 Ma (Fig. 7d).

400 Similarly, one hundred zircon grains from the Middle Jurassic sample
401 KZLT1602 exhibit characteristics indicative of a magmatic origin, with high Th/U
402 ratios ranging between 0.11 and 2.63 (Fig. 5d). Ninety - eight concordant results
403 display consistent age population with the sample KZLT1601, ranging from 345
404 ± 4 Ma to 3029 ± 15 Ma (Fig. 7e). These age populations on the KDE plot also
405 display four main peaks at approximately 435 Ma, 782-988 Ma, 1829 Ma, and
406 2480 Ma (Fig. 7f).

407

408 **4.4 Analysis of Jurassic conglomerate clast lithologies**

409 The field provenance analysis of the Lower Jurassic conglomerate
410 (Shalitashi Formation) reveals significant variations in composition across
411 different sections. In the Kangsu and Wulagen sections, located in the
412 northernmost region of the West Kunlun Range, clasts are composed
413 predominantly of green-colored sandstone (80-51%) and low-grade
414 metamorphic rocks like schist (0-46%), with minor occurrences of light-colored
415 siliceous rock (14-3%) and granitoid (6-0%). In the northwestern sector of the
416 Pamir, sandstone (22-46%) and recycled siliceous rock (29-46%)
417 predominantly constitute major clasts in the Oyttag and Gaizi sections,
418 respectively (Fig. 3b and 3c). Additionally, minor limestone (11-2%) and diverse
419 igneous rocks (38-6%), including granitoid, rhyolite, and basalt occur
420 characteristically in the same stratigraphic horizon. In the Kyzyltau section (Fig.
421 3d), the clasts of the Jurassic conglomerate are dominated by green-colored
422 sandstone (28%) and granite (50%) with subordinate schist (13%) and siliceous
423 rock (9%). To the south of Kyzyltau, the Tamu and Qimugen sections present a
424 provenance source dominated by sedimentary rocks. Clasts of limestone (Fig.
425 3e) and green-colored sandstone account for 85% and 61% in the neighboring
426 sections, respectively. The proportion of reddish sandstone in the Qimugen
427 section (33%) surpasses that in the Tamu section (15%). The Kusilafu section,
428 located to the north of the Kandilik region, exhibits similar clast lithologies in the
429 conglomerate to the Qimugen section, with a predominance of green-colored
430 sandstone (34%) and recycled siliceous rock (45%), along with minor
431 occurrences of reddish sandstone (16%). Detailed clast lithologies and

432 counting results are presented in the Table S5.

433

434 **5 Identification and age constraints for the Lower Jurassic strata**

435 Jurassic strata are largely exposed in the eastern edge of the West Kunlun
436 Mountains and on the southern side along the Talas-Fergana Fault (Fig. 1c).

437 The Jurassic sequences are comprised of coal-bearing siliciclastic rocks with
438 variable thicknesses (Wu et al., 2021). Jurassic volcanic strata have not been
439 previously identified in the West Kunlun Mountains, although a Jurassic
440 tuffaceous succession and Upper Triassic - Lower Jurassic volcanic rocks crop
441 out in the Hindu Kush along the western edge of the Pamir (Brookfield and
442 Hashmat, 2001). Our study has focused on a package of thick clastic rocks
443 intercalated with basaltic lavas, exposed in the southernmost part of the
444 Jurassic Kyzyltau syncline (Fig. 2). This stratigraphic package was previously
445 considered to be of Mesoproterozoic or Neoproterozoic age due to the lack of
446 fossil records and the presence of low-degree metamorphism (Ma et al., 1991).
447 Lithologically, the clastic member is composed primarily of gray-black mudstone
448 and fine - grained sandstone to siltstone, rich in iron and carbonaceous
449 components (Ma et al., 1991). The overlying basalts vary significantly in their
450 thickness and lithological composition, composed primarily of basaltic volcanic
451 breccia, amygdaloidal, and massive layers (Fig.3j and 3k).

452 Our new results of zircon U-Pb dating of basalts and sandstones suggest
453 that this rock assemblage is not Precambrian in age, given the widespread
454 appearance of Phanerozoic ages. We suggest that the weighted mean
455 $^{206}\text{Pb}/^{238}\text{U}$ age (~178 Ma) from the basalt sample could define the eruptive age
456 of this magmatic episode based on the following lines of evidence. First, these

457 zircons exhibit similar morphological and CL imaging characteristics (Fig. 4),
458 with the majority of the analyzed grains displaying Th/U ratios indicating their
459 igneous origin (Fig. 5d). Secondly, the results of our in-situ trace elemental
460 composition of the zircons (Table S3) indicate that the chondrite-normalized
461 rare earth elements consistently exhibit left-sloping pattern with positive
462 anomalies in Ce and Sm, and negative anomalies in Eu, similar to those of
463 typical igneous zircons (Fig. 5c; Hoskin and Schaltegger, 2003). Thirdly,
464 according to the Y vs. Yb/Sm plot proposed by Belousova et al. (2002), these
465 Jurassic zircons are consistent with the basic or ultrabasic igneous origin (Fig.
466 5e). Thus, we posit that the crystallization age of the basalt is Toarcian.

467 To refine the depositional age of the clastic member of the stratigraphy, we
468 have compared the detrital zircon results from the feldspar lithic sandstones
469 with those from the Lower and Middle Jurassic strata in the Kyzyltau region.
470 The sandstone collected from the Kangsu Formation displayed similar texture
471 and composition to the rocks from the Kandilik region, both composed of
472 immature and poorly sorted quartz and lithic fragments (Fig. 3n and 3o). The
473 age patterns of detrital zircons display remarkably similar populations with Early
474 Silurian (~440 Ma) and Tonian (~800-950 Ma) peaks, indicating that sediments
475 of the two investigated areas shared a common provenance. The Lower and
476 Middle Jurassic sedimentary rocks were previously suggested to have been
477 deposited within half grabens and mostly sourced from the West Kunlun
478 Mountains (Chen et al., 2018). This interpretation aligns with our findings, which
479 indicate that this stratigraphic package comprises thick sequences of laminated
480 mudstone and siltstone, resembling rift-related deposits formed in a relatively
481 proximal, rapidly filling depositional environment.

482 Accordingly, we propose reassigning this thick package of clastic rocks to
483 the Early - Middle Jurassic age. We demonstrate the structural compatibility of
484 this new stratigraphic scheme. The Lower to Middle Jurassic strata of the
485 Yarkant Formation in the study area consist of a lacustrine sequence rich in
486 coal beds, structurally bounded to the west by a mylonite zone (Fig. 2b). The
487 redefined stratigraphic sequence is similarly rich in carbonaceous material and
488 is thrust beneath the coal-bearing strata of the Yarkant Formation along an
489 east-verging thrust fault. These units could extend into the NW-SE-striking
490 Jurassic graben, which surprisingly narrows rapidly towards the south without
491 any obvious facies transition (Fig. 1c). The basin-ward dipping of strata
492 constituted the western limb of the Jurassic syncline, which has a comparable
493 thickness that may extend into the southern area of the Kyzyltau syncline (Fig.
494 2).

495

496 **6 Discussion**

497 **6.1 Tectonic setting of the Early Jurassic volcanism**

498 The varying SiO₂ contents and low Mg# values of the basalt samples
499 suggest that they were not derived from primary magmas but likely underwent
500 crustal assimilation and fractional crystallization (AFC) processes. Generally,
501 mantle-derived magmas suffer various degrees of crust contamination en-route
502 from magma chambers to the surface (Aitcheson and Forrest, 1994). The
503 presence of inherited Paleozoic and Neoproterozoic zircons in these basalts
504 suggests the potential interactions between the ascending magmas and the
505 country rocks (Fig. 5a). However, these basaltic rocks exhibit no negative
506 anomalies of Nb, Ta, and Ti, which are typically depleted in the crust (Fig. 6d).

507 They exhibit low La/Nb ratios (0.53 - 1.15) and mostly have high Nb/U ratios
508 (37 - 45), similar to the range of oceanic lavas (La/Nb <1.2 and Nb/U >39;
509 Krienitz et al., 2006). Additionally, all basalt samples exhibit low Th/Nb ratios
510 (0.09-0.15), plotting along the MORB–OIB array of oceanic basalts within the
511 Th/Yb-Nb/Yb diagram (Fig. 6e; Pearce, 2008). These signatures, with little
512 indication of crustal components, suggest that these basalts experienced
513 negligible crustal contamination. They show extremely low Ni and Cr
514 concentrations and slight negative Eu and Sr anomalies (Fig. 6c-d), likely
515 resulting from fractional crystallization of olivine, clinopyroxene, and plagioclase.

516 The Early Jurassic episode (178 Ma) of volcanism in the West Kunlun
517 Mountains temporally followed the Cimmerian Orogeny. The eruption of the
518 Early Jurassic basalts was slightly later than the peak metamorphism of high-
519 pressure granulite facies that has been proposed to have occurred between
520 200 and 185 Ma (Qu et al., 2021). Collisional orogeny commonly transitions
521 from syn-collisional metamorphism to post-collisional unroofing (Dilek and
522 Altunkaynak, 2007, 2010; Zheng et al., 2019). The unroofing phase could
523 generate geochemically varying granitoids and mafic magmatic rocks (Harris et
524 al., 1986; Zhou et al., 2021).

525 The Jurassic alkali basalts exhibit enrichment of LREE and HSFES without
526 obvious crustal signatures (Fig. 6c-d), different from the syn-/post-collisional
527 mafic intrusions and granitoids in the West Kunlun Mountains (Liao et al., 2012;
528 Chen et al., 2021). Their compositions display high Th/Yb and Nb/Yb ratios,
529 similar to intraplate OIBs (Fig. 6e). Melt curve modeling of La/Sm vs. La
530 suggests they were likely generated by low-degree partial melting (~5%) of a
531 garnet lherzolite mantle source (Fig. 7f). This aligns with the Zr-Nb-Y and Zr-Y-

532 Ti triangular plots proposed by Meschede (1986), indicating a within-plate
533 affinity for the studied Jurassic basalts (Fig. 8a-b). They also have high Ti-Zr
534 contents and Ti/V ratios (48-77), consistent with the characteristics of within-
535 plate alkali basalts or OIBs (Fig. 8d-e).

536 The generation of these magmas can be attributed to one of two
537 mechanisms. The first explanation is that the North Kunlun region experienced
538 rapid orogenic collapse after Late Triassic collisional orogeny, during which
539 intra-plate collapse-related volcanism generate the observed basalt flows. We
540 do not find this hypothesis plausible given the implied rapid transition from peak
541 collisional orogeny, including ca. 185 Ma prograde metamorphism (Qu et al.,
542 2021), to collapse and volcanism recorded at ca. 178 Ma. Many arc-continent
543 or continent-continent collisional orogens, evolving from peak orogenic
544 metamorphism, to orogenic collapse, to intraplate stage, collectively persist for
545 tens of millions of years (Dewey, 2005; Weller et al., 2021). Conversely, Early-
546 Middle Jurassic graben and half-graben structures are widely identified by
547 seismic profiles in the southwestern and southeastern Tarim Basin, and Qaidam
548 Basin (Cheng et al., 2019; Zhao et al., 2020; Wu et al., 2021; Xia et al., 2024).
549 Jurassic extensional faults have been reported in the eastern Altyn Tagh Range
550 (Chen et al., 2003). A broad plate-boundary extensional process may have
551 impacted these orogenic belts and their hinterland regions. Support for this
552 model also includes the expansive extensional rifts developed across the
553 marginal and interior Eurasia during the Early-Middle Jurassic (e.g., Amu-
554 Dar'ya, Afghan-Tajik and Fergana basins; Otto, 1997; Golonka, 2004).

555

556 **6.2 Jurassic basin formation and implications for sedimentary**

557 **provenance**

558 The Late Triassic closure of the Paleo-Tethyan Ocean led to collision of the
559 Cimmerian terranes with Eurasia that caused the uplift of the West Kunlun
560 Mountains (Cao et al., 2015). The Triassic stratum is completely absent in the
561 North Kunlun region and western Tarim Basin (Wu et al., 2021). In the study
562 area, the deformed Upper Paleozoic strata are unconformably overlain by
563 Lower Jurassic conglomerates (Fig. 9).

564 The Kyzyltau basin preserves the most comprehensive record of the
565 formation and evolution of a post-Cimmerian rift, spanning from its initiation in
566 the Early Jurassic to its inversion in the Late Jurassic (Wu et al., 2021). The
567 basement of this basin varies along-strike, indicating its strong tectonic
568 reworking prior to Jurassic deposition. It comprises four subdivisions from the
569 north to the southeast: (1) an Early Devonian metasedimentary rock terrane in
570 the Kashgar depression (1-4 in Fig. 9), (2) the Carboniferous island-arc crust
571 and Permian back-arc basin successions in the NW segment of the West
572 Kunlun (5-6 in Fig. 9), (3) an Upper Carboniferous to Middle Permian platform
573 successions in the middle segment (7-11 in Fig. 9), and (4) an Upper Permian
574 clastic formation in the southern part (12-17 in Fig. 9). The massive
575 conglomerate of the Shalitashi Formation indicates rapid infilling of the Jurassic
576 basin during its initial opening stage. Analysis of conglomerate clast lithologies
577 from different sites suggests significant compositional variations, consistent
578 with the presence of local basement rocks (Fig. 9).

579 The Lower Jurassic strata rapidly transition from alluvial fan deposits into
580 fluvial sedimentary environment. During the Middle Jurassic, a sequence of
581 stacked coal-bearing sandstones was deposited (Fig. 9). Extensional faulting

582 across the half-grabens further deepened the basin and facilitated the
583 deposition of a turbidite sequence in the Yangye Formation (Wu et al., 2021).
584 Provenance analysis based on detrital zircons suggests that the source region
585 for these sandstones was dominated by Late Ordovician-Early Silurian (~ 446
586 - 435 Ma) and Neoproterozoic (~ 980 - 780 Ma) igneous rocks, with minor
587 Neoproterozoic and Mesoproterozoic ages (Fig. 7). Early
588 Paleozoic (~ 480 - 440 Ma) granitoids, with a peak intrusive event at ~ 440 Ma
589 (Fig. 1c; Tao et al., 2024), are exposed extensively in the South Kunlun terrane.
590 However, the South Kunlun terrane is unlikely to be the source for these
591 Jurassic depositions because the South Kunlun region contains extensive
592 Triassic (~ 240 - 210 Ma) granitoids, intruded into the early Paleozoic rock units
593 (Fig. 1c; Chen et al., 2021). Yet, Triassic detrital zircons are absent in the Lower
594 - Middle Jurassic strata (Fig. 7). Therefore, we instead suggest that the potential
595 source area was most likely the North Kunlun terrane, which consists mainly of
596 Paleozoic strata and Precambrian metamorphic basements. A provenance
597 study has revealed that the age patterns of detrital zircons from the Ordovician
598 - Devonian strata contain main age peaks at 430 - 445 Ma, 930 - 800 Ma, and
599 790 - 760 Ma, with subordinate Neoproterozoic to Mesoproterozoic ages (Yan,
600 2022). Our results are consistent with this detrital zircon age information from
601 the Lower Paleozoic sedimentary rocks and with the paleocurrent results of
602 previous studies (Wu et al., 2021).

603 A Late Jurassic contractional event affected this region, as evidenced by
604 the intense deformation and metamorphism displayed by various formations
605 and rock units in orogen (Robinson et al., 2007; Groppo et al., 2019), and by
606 the uplift and inversion of the earlier basin (Yang et al., 2017). The Middle

607 Jurassic shallow marine sequences in South Qiangtang and SE Pamir were
608 uniformly eroded during this time period (Ma et al., 2023). The Upper Jurassic
609 strata are either entirely absent or locally replaced by conglomerate deposits
610 (Fig. 10). In the Tarim Basin, the Upper Jurassic strata are dominated by
611 brownish reddish conglomerate. Previous studies have suggested that these
612 redbeds may indicate a regional increase in aridity resulting from the uplift of
613 the surrounding mountain belts (Hendrix, 2000). The Late Jurassic uplift event
614 has also been supported by numerous thermochronologic ages (170-155 Ma)
615 within the West Kunlun Mountains and Pamir (Fig.1c; Yang et al., 2017). The
616 uplift event also resulted in significant changes in basin and range patterns, and
617 influenced the potential provenance of sediments. The emergence of juvenile
618 detrital zircons in these Upper Jurassic and Lower Cretaceous deposits
619 indicates the exhumation and erosion of a late Paleozoic to Mesozoic arc
620 system (Fig. 10). The Triassic batholiths were thrust onto the southwestern
621 margin of the Tarim Basin and generated elevated topography, which supplied
622 igneous clastic material to the Cretaceous depocenters in the region.

623 In summary, the Early Jurassic basin developed on the deformed
624 Paleozoic basement, separated by the Triassic orogenic unconformity.
625 Provenance analysis indicates that the Early to Middle Jurassic sediments were
626 deposited in a half-graben setting and sourced from the proximal basement of
627 the North Kunlun terrane. This basin was subsequently inverted during the Late
628 Jurassic, driven by the contraction and uplift of the surrounding mountains.

629

630 **6.3 Switching extensional and contractional tectonics related to the** 631 **subduction of Neo-Tethys**

632 The Mesozoic era records the transition from the closure of the Paleo-
633 Tethys Ocean to the initiation of subduction within Neo-Tethys (Wan et al., 2019).
634 These processes are influenced by complex plate tectonic conditions, as the
635 evolution of the Paleo- and Neo-Tethys Oceans varies significantly in their time-
636 space patterns. The two Tethyan oceans diverge into several branches
637 extending from Iran to Pamir, then eastward into the Tibetan Plateau (Fig. 1a).

638 Episodic collisions along the southern Asian margin in the Late Triassic and
639 then in the Late Jurassic resulted in major deformation in this region (Jolivet,
640 2017). Although a flat subduction model has recently been proposed to explain
641 the regional Cretaceous magmatism in the Pamir, the mode of Jurassic tectonic
642 processes remains poorly constrained (Chapman et al., 2018). As discussed
643 above, the history of the Neo-Tethyan subduction events significantly varies
644 spatially. The initiation of subduction along the Tibetan margin occurred during
645 the Middle Triassic, leading to volcanic activities in the southern Lhasa (Wang
646 et al., 2016; Xie et al., 2021), whereas the subduction in the Iran sector in the
647 same orogenic belt farther west initiated later in the Early Jurassic (Wan et al.,
648 2023). The extensive Early-Middle arc Jurassic magmatism along both
649 continental margins indicates a synchronous flare-up of continental arcs (Fig.
650 11a and 11c). The bimodal volcanism (195-174 Ma) in the Gangdese arc was
651 associated with the subsequent opening of a back-arc basin (174-156 Ma) (Fig.
652 11c; Kapp and DeCelles, 2019). The magmatic arc of the Sanandaj–Sirjan belt
653 (180-140 Ma) in SW Iran was facilitated by a simultaneous progressive back-
654 arc rift (Fig. 11a; Hassanzadeh and Wernicke, 2016; Azizi and Stern, 2019).

655 By comparison, compiled magmatic detrital zircons in the Pamir segment
656 reveal that Early-Middle Jurassic magmatism was almost absent (Fig. 11b;

657 Chapman et al., 2018). Jurassic igneous rocks surrounding the Pamir are also
658 limited (Fig. 7), with only basalts exposed in the North Kunlun (Kandilik) and
659 Tianshuihai regions (Jian et al., 2019) and bimodal volcanic rock suites found
660 in the east of Karakoram (Zhou et al., 2019). These coeval basaltic lavas (178-
661 174 Ma) exhibit distinct features in their major and trace element compositions
662 (Fig. 6). Magmas of the basaltic lavas in the North Kunlun were dominated by
663 within-plate OIBs (Fig. 6 and 8). In contrast, basalts in the Tianshuihai to the
664 south were dominated by back-arc MORBs (Fig. 8a-c), characterized by distinct
665 Nb-Ta depletions (Fig. 6d). The scarcity of zircon-rich felsic magmas in this
666 region evidently differs from the conditions in the western and eastern
667 segments of the Eurasian Tethyan margins where arc magmatism developed
668 upon continental basement. To date, the exact timing of the onset of
669 subduction-related magmatism in the Pamir Tethyan margin remains unclear.
670 The geochronological dataset for the Karakoram arc and the Kohistan Ladakh
671 arc indicates that magmatic activity may have occurred as early as the Late
672 Jurassic (Fig. 11b; Jagoutz et al., 2018; Saktura et al., 2023).

673 While the spatial continuity of the Tethyan suture zones from Iran into Tibet
674 remains enigmatic, we propose that the regional Early to Middle Jurassic
675 extension across the southern Eurasian continental margin was a consequence
676 of retreating subduction of the Neo-Tethyan Ocean floor. First, the transition
677 from Cimmerian orogenic build-up (200-185 Ma) to large-scale continental
678 extension (178-174 Ma) suggests the involvement of additional external
679 extensional stresses, different from the classic cases of continent - continent
680 collision (Weller et al., 2021). Secondly, the 195 Ma bimodal volcanic rocks in
681 Karakoram and the 174 Ma MORB-like basalts in Tianshuihai have been

682 suggested as associated with the initial opening of a back-arc basin, based on
683 their geochemical signatures of crustal material metasomatism (Jian et al.,
684 2019; Zhou et al., 2019). The magmatism in Pamir and Karakoram was quite
685 similar to the extensional episodes that occurred in the southern margin of the
686 Lhasa block, caused by accelerated slab rollback (Kapp and DeCelles, 2019).
687 Thirdly, deposition of shallow marine carbonates was prevalent in the Pamir
688 and Karakoram during the Middle Jurassic (Fig. 10), indicating an expansive
689 extensional continental platform facing the ocean (Yang et al., 2017). These
690 scenarios are analogous to the active margin of the western Pacific rim, which
691 is characterized by a broad marginal sea with an outboard trench - subduction
692 chain (Fig. 1a). Additionally, the Middle Jurassic extension occurred across the
693 broad hinterlands of central Asia, which cannot be easily explained by the
694 collapse of the Paleo-Tethyan orogenic belt (Otto, 1997).

695 During the Late Jurassic, this marginal extensional basin started to invert,
696 with extensive contractional deformation of the Lower-Middle Jurassic
697 carbonate strata and the development of a major angular unconformity (Fig. 10;
698 Gaetani et al., 1993; Robinson, 2015). Available basement thermochronological
699 data show widespread exhumation across the West Kunlun Mountains (Fig. 1c),
700 as well as the reactivation of the Paleo-Tethyan sutures within the Pamir
701 terranes (Schwab et al., 2004). The exhumation of the Triassic plutons in the
702 South Kunlun Mountain led to the transport of debris material from the
703 magmatic arc into the Tarim basin through braided fluvial network systems (Fig.
704 11b). This broad uplift event has been interpreted as retro-arc deformation and
705 shortening related to the advancing subduction of the Neo-Tethyan Ocean
706 (Robinson, 2015).

707 The subduction style along the broader strike-length of the Tethyan orogen
708 varied from the west to the east in the Late Jurassic - Early Cretaceous. Similar
709 to the West Kunlun Mountains, the Lhasa block to the east experienced basin
710 inversion and contractional deformation starting by ca. 155 Ma and throughout
711 the Early Cretaceous (e.g., Murphy et al., 1997; Ding and Lai, 2003; Kapp and
712 DeCelles, 2019). Geological mapping has documented significant shortening
713 strain (~ 60%) across Lhasa at this time (Murphy et al., 1997). Although the
714 cause of this event has been debated, the magmatic lull since the earliest
715 Cretaceous and subsequent flare-up in the Mid-Cretaceous in both regions
716 imply that they shared a similar geodynamic setting (Fig. 11; Chapman et al.,
717 2018). A major tectonic event involving intense folding and thrusting occurred
718 also around 166 Ma in the South Qiangtang Block, resulting in two phases of
719 southward retreat of the remnant seaway of the Meso-Tethys (Ma et al., 2017a,
720 2018). A previous study proposed that the development of Jurassic basin
721 inversion in the Tibetan Plateau may be related to the accretion of
722 microcontinents onto the South Qiangtang margin, driven by the northward
723 subduction of the Bangong-Nujiang Ocean (Ma et al., 2023). Conversely, the
724 Iranian segment to the west experienced continuous extension at the same time
725 (Hunziker et al., 2015; Lechmann et al., 2018; Maghdour-Mashhour et al., 2021).
726 These along-strike variations likely reflect broad geodynamic changes to, or
727 initial conditions of, the Tethyan Ocean system that warrant future investigations.
728 For example, variable plate convergence rates related to global tectonic
729 configurations or the oceanic-plate age variations could result in unique tectonic
730 events along the strike-length of the entire Tethyan orogen. Alternatively, the
731 closure of the Bangong-Nujiang Ocean, another branch of the Tethyan system

732 between the Lhasa and Qiangtang blocks, might have also played a significant
733 role in along-strike variations within the Tethyan orogenic belt (Fig. 11; Yang et
734 al., 2017; Kapp and DeCelles, 2019).

735

736 **7 Conclusion**

737 This study has concentrated on the stratigraphy and provenance of
738 Jurassic strata in the West Kunlun Mountains to better understand the
739 Mesozoic geological evolution of the Eurasian margin within the framework of
740 the Tethyan geodynamics. Our investigations of the Jurassic sedimentary
741 successions, combined with new geochronological and geochemical data from
742 coeval basaltic lava intercalations, led to the following conclusions:

743 (1) A newly identified, thick sedimentary package with basaltic lava
744 interlayers in the southern end of the Kyzyltau basin bears similarities to the
745 Lower and Middle Jurassic sequences in their clastic compositions and
746 structures. Zircon U-Pb dating results from basaltic lavas suggest an Early
747 Jurassic age (~ 178 Ma) for this stratigraphic member, in contrast to a
748 Precambrian age previously reported. This is a significant change that strongly
749 affects the current tectonic interpretations and models.

750 (2) Our new geochemical data from the Early Jurassic basaltic extrusive
751 rocks show that magmas of these basalts had typical OIB affinities, and that
752 they lacked crustal contamination. Thus, the related magmatism likely occurred
753 in an intraplate rifting setting and was facilitated by extensional fault systems,
754 which significantly reduced the residence time of the ascending magmas in the
755 crust avoiding contamination.

756 (3) Provenance analysis, integrating conglomerate clast lithologies with

757 detrital zircons, indicates a significant source contribution from local basements
758 (North Kunlun) for the Early to Middle Jurassic rift basins. In comparison, the
759 Late Jurassic contractional event caused an uplift of the surrounding mountains
760 in the South Kunlun and Pamir, significantly influencing the basin
761 tectonostratigraphy and source- to -sink system.

762 (4) The Jurassic switching extensional and contractional tectonics in the
763 West Kunlun Mountains and a wider region across the southern Eurasian
764 margin are related to changes in the subduction style of the Neo-Tethyan Ocean
765 floor, transitioning from retreating in Early - Middle Jurassic to advancing in Late
766 Jurassic - Early Cretaceous. Additionally, the Pamir and West Kunlun regions,
767 as the central junction of the Tethys orogenic belt, share a comparable
768 Mesozoic history of extensional and contractional structures with that of the
769 Tibetan Plateau.

770

771 **Declaration of Competing Interest**

772 The authors declare that they have no known competing financial interests
773 or personal relationships that could have appeared to influence the work
774 reported in this paper.

775

776 **Acknowledgement**

777 We gratefully acknowledged the constructive and insightful reviews by two
778 anonymous reviewers and topic editor Yang Chu, and the effective editorial
779 handling of Federico Rossetti. This work was supported by the National Natural
780 Science Foundation of China (Grants No. U22B6002 and 42302231). H.-X. Wu
781 received the funding of Postdoctoral Science Foundation (2023M742979 and
782 2024T170768).

783

784 **Author Contributions**

785 *Hong-Xiang Wu*: Conceptualization, Formal Analysis, Investigation,
786 Methodology, Visualization, Writing – original draft, Writing – review & editing,
787 Funding acquisition; *Han-Lin Chen*: Funding acquisition, Investigation, Project
788 administration; *Andrew V. Zuza*: Writing – review & editing; *Yildirim Dilek*:
789 Writing – review & editing; *Du-Wei Qiu*: Investigation, Formal Analysis; *Qi-Ye*
790 *Lu*: Investigation, Formal Analysis; *Feng-Qi Zhang*: Investigation, Formal
791 Analysis; *Xiao-Gan Cheng*: Investigation; *Xiu-Bin Lin*: Investigation.

792

793 **Data availability**

794 The data used in this study are available in the references and
795 Supplementary Material, including five tables and one figure.

796

797 **References**

798 Aldanmaz, E., Pearce, J. A., Thirlwall, M. F., and Mitchell, J. G.: Petrogenetic
799 evolution of late Cenozoic, post-collision volcanism in western Anatolia,
800 Turkey, *Journal of Volcanology and Geothermal Research*, 102, 67-95,
801 [https://doi.org/10.1016/S0377-0273\(00\)00182-7](https://doi.org/10.1016/S0377-0273(00)00182-7), 2000.

802 Andersen, T.: Correction of common lead in U–Pb analyses that do not report
803 ^{204}Pb , *Chemical Geology*, 192, 59-79, [https://doi.org/10.1016/S0009-](https://doi.org/10.1016/S0009-2541(02)00195-X)
804 [2541\(02\)00195-X](https://doi.org/10.1016/S0009-2541(02)00195-X), 2002.

805 Angiolini, L., Zanchi, A., Zanchetta, S., Nicora, A., Vuolo, I., Berra, F.,
806 Henderson, C., Malaspina, N., Rettori, R., Vachard, D., and Vezzoli, G.:
807 From rift to drift in South Pamir (Tajikistan): Permian evolution of a
808 Cimmerian terrane, *Journal of Asian Earth Sciences*, 102, 146-169,
809 <https://doi.org/10.1016/j.jseaes.2014.08.001>, 2015.

810 Angiolini, L., Zanchi, A., Zanchetta, S., Nicora, A., and Vezzoli, G.: The
811 Cimmerian geopuzzle: new data from South Pamir, *Terra Nova*, 25, 352-
812 360, <https://doi.org/10.1111/ter.12042>, 2013.

813 Aitchison, S. J. and Forrest, A. H.: Quantification of Crustal Contamination in
814 Open Magmatic Systems, *Journal of Petrology*, 35, 461-488,
815 [10.1093/petrology/35.2.461](https://doi.org/10.1093/petrology/35.2.461), 1994.

816 Azizi, H. and Stern, R. J.: Jurassic igneous rocks of the central Sanandaj–Sirjan
817 zone (Iran) mark a propagating continental rift, not a magmatic arc, *Terra*
818 *Nova*, 31, 415-423, <https://doi.org/10.1111/ter.12404>, 2019.

819 Belousova, E., Griffin, W., O'Reilly, S. Y., and Fisher, N.: Igneous zircon: trace
820 element composition as an indicator of source rock type, *Contributions to*
821 *Mineralogy and Petrology*, 143, 602-622, [10.1007/s00410-002-0364-7](https://doi.org/10.1007/s00410-002-0364-7),

822 2002.

823 Brookfield, M. E. and Hashmat, A.: The geology and petroleum potential of the
824 North Afghan platform and adjacent areas (northern Afghanistan, with parts
825 of southern Turkmenistan, Uzbekistan and Tajikistan), *Earth-Science*
826 *Reviews*, 55, 41-71, [https://doi.org/10.1016/S0012-8252\(01\)00036-8](https://doi.org/10.1016/S0012-8252(01)00036-8),
827 2001.

828 Burtman, V. S. and Molnar, P.: Geological and Geophysical Evidence for Deep
829 Subduction of Continental Crust Beneath the Pamir, in: *Geological and*
830 *Geophysical Evidence for Deep Subduction of Continental Crust Beneath*
831 *the Pamir*, Geological Society of America, 0, 10.1130/SPE281-p1, 1993.

832 Cabanis, B. and Lecolle, M.: The La/10-Y/15-Nb/8 diagram: a tool for
833 discriminating volcanic series and evidencing continental crust magmatic
834 mixtures and/or contamination, *Comptes Rendus - Academie des*
835 *Sciences, Serie II*, 309, 2023-2029, 1989.

836 Cao, K., Wang, G.-C., Bernet, M., van der Beek, P., and Zhang, K.-X.:
837 Exhumation history of the West Kunlun Mountains, northwestern Tibet:
838 Evidence for a long-lived, rejuvenated orogen, *Earth and Planetary*
839 *Science Letters*, 432, 391-403, <https://doi.org/10.1016/j.epsl.2015.10.033>,
840 2015.

841 Cao, W., Zahirovic, S., Flament, N., Williams, S., Golonka, J., and Müller, R. D.:
842 Improving global paleogeography since the late Paleozoic using
843 paleobiology, *Biogeosciences*, 14, 5425-5439, 10.5194/bg-14-5425-2017,
844 2017.

845 Chapman, J. B., Scoggin, S. H., Kapp, P., Carrapa, B., Ducea, M. N.,
846 Worthington, J., Oimahmadov, I., and Gadoev, M.: Mesozoic to Cenozoic

847 magmatic history of the Pamir, *Earth and Planetary Science Letters*, 482,
848 181-192, <https://doi.org/10.1016/j.epsl.2017.10.041>, 2018.

849 Chen, X., Yin, A., Gehrels, G. E., Cowgill, E. S., Grove, M., Harrison, T. M., and
850 Wang, X.-F.: Two phases of Mesozoic north-south extension in the eastern
851 Altyn Tagh range, northern Tibetan Plateau, *Tectonics*, 22,
852 <https://doi.org/10.1029/2001TC001336>, 2003.

853 Chen, S., Chen, H., Zhu, K., and Tao, Y.: Petrogenesis of the Middle–Late
854 Triassic S- and I-type granitoids in the eastern Pamir and implications for
855 the Tanyamas–Jinshajiang Paleo-Tethys Ocean, *International Journal of*
856 *Earth Sciences*, 110, 1213-1232, 10.1007/s00531-021-02013-z, 2021.

857 Chen, Y., Wu, H., Zhang, L., Cheng, X., Chen, C., Zhang, Y., Ren, P., Zhang, F.,
858 and Chen, H.: Characteristics of the Late Triassic paleo-structure in the
859 mountain front region of western Kunlun and its control of Jurassic-
860 Cretaceous deposition, *Chinese Journal of Geology*, 53, 1405-1418, 2018
861 (in Chinese with English abstract).

862 Cheng, F., Jolivet, M., Guo, Z., Lu, H., Zhang, B., Li, X., Zhang, D., Zhang, C.,
863 Zhang, H., Wang, L., Wang, Z., and Zhang, Q.: Jurassic–Early Cenozoic
864 Tectonic Inversion in the Qilian Shan and Qaidam Basin, North Tibet: New
865 Insight From Seismic Reflection, Isopach Mapping, and Drill Core Data,
866 *Journal of Geophysical Research: Solid Earth*, 124, 12077-12098,
867 <https://doi.org/10.1029/2019JB018086>, 2019.

868 Corfu, F., Hanchar, J. M., Hoskin, P. W. O., and Kinny, P.: Atlas of Zircon
869 Textures, *Reviews in Mineralogy and Geochemistry*, 53, 469-500,
870 10.2113/0530469, 2003.

871 Cowgill, E.: Cenozoic right-slip faulting along the eastern margin of the Pamir

872 salient, northwestern China, GSA Bulletin, 122, 145-161,
873 10.1130/b26520.1, 2010.

874 Dewey, J. F.: Orogeny can be very short, Proceedings of the National Academy
875 of Sciences, 102, 15286-15293, doi:10.1073/pnas.0505516102, 2005.

876 Dilek, Y. and Altunkaynak, Ş.: Cenozoic Crustal Evolution and Mantle Dynamics
877 of Post-Collisional Magmatism in Western Anatolia, International Geology
878 Review, 49, 431-453, 10.2747/0020-6814.49.5.431, 2007.

879 Dilek, Y. and Altunkaynak, Ş.: Geochemistry of Neogene–Quaternary alkaline
880 volcanism in western Anatolia, Turkey, and implications for the Aegean
881 mantle, International Geology Review, 52, 631-655,
882 10.1080/00206810903495020, 2010.

883 Dilek, Y. and Furnes, H.: Tethyan ophiolites and Tethyan seaways, Journal of
884 the Geological Society, 176, 899-912, doi:10.1144/jgs2019-129, 2019.

885 Dilek, Y. and Moores, E. M.: Regional tectonics of the eastern Mediterranean
886 ophiolites. In: J. Malpas, E. M. Moores, A. Panayiotou, and C. Xenophontos
887 (Eds), Ophiolites. Oceanic Crustal Analogues, Proceedings of the
888 Symposium “Troodos 1987”, The Geological Survey Department, Nicosia,
889 Cyprus, 295–309, 1990.

890 Ding, L. and Lai, Q.: New geological evidence of crustal thickening in the
891 Gangdese block prior to the Indo-Asian collision, Chinese Science Bulletin,
892 48, 1604-1610, 10.1007/BF03183969, 2003.

893 Dong, Y., He, D., Sun, S., Liu, X., Zhou, X., Zhang, F., Yang, Z., Cheng, B.,
894 Zhao, G., and Li, J.: Subduction and accretionary tectonics of the East
895 Kunlun orogen, western segment of the Central China Orogenic System,
896 Earth-Science Reviews, 186, 231-261,

897 <https://doi.org/10.1016/j.earscirev.2017.12.006>, 2018.

898 Faisal, S., Larson, K. P., Cottle, J. M., and Lamming, J.: Building the Hindu Kush:
899 monazite records of terrane accretion, plutonism and the evolution of the
900 Himalaya–Karakoram–Tibet orogen, *Terra Nova*, 26, 395-401,
901 <https://doi.org/10.1111/ter.12112>, 2014.

902 Gaetani, M., Jadoul, F., Erba, E., and Garzanti, E.: Jurassic and Cretaceous
903 orogenic events in the North Karakoram: age constraints from sedimentary
904 rocks, *Geological Society, London, Special Publications*, 74, 39-52,
905 doi:10.1144/GSL.SP.1993.074.01.04, 1993.

906 Golonka, J.: Plate tectonic evolution of the southern margin of Eurasia in the
907 Mesozoic and Cenozoic, *Tectonophysics*, 381, 235-273,
908 <https://doi.org/10.1016/j.tecto.2002.06.004>, 2004.

909 Groppo, C., Rolfo, F., McClelland, W. C., and Coble, M. A.: Pre-Cenozoic
910 evolution of the Aghil Range (western Tibetan Plateau): A missing piece of
911 the Tibet-Pamir-Karakorum geopuzzle, *Gondwana Research*, 69, 122-143,
912 <https://doi.org/10.1016/j.gr.2018.12.006>, 2019.

913 Guo, P., Niu, Y., Sun, P., Gong, H., and Wang, X.: Lithosphere thickness
914 controls continental basalt compositions: An illustration using Cenozoic
915 basalts from eastern China, *Geology*, 48, 128-133, 10.1130/g46710.1,
916 2020.

917 Harris, N. B. W., Pearce, J. A., and Tindle, A. G.: Geochemical characteristics
918 of collision-zone magmatism, *Geological Society, London, Special
919 Publications*, 19, 67-81, doi:10.1144/GSL.SP.1986.019.01.04, 1986.

920 Hassanzadeh, J. and Wernicke, B. P.: The Neotethyan Sanandaj-Sirjan zone
921 of Iran as an archetype for passive margin-arc transitions, *Tectonics*, 35,

922 586-621, <https://doi.org/10.1002/2015TC003926>, 2016.

923 Hendrix, M. S.: Evolution of Mesozoic Sandstone Compositions, Southern
924 Junggar, Northern Tarim, and Western Turpan Basins, Northwest China: A
925 Detrital Record of the Ancestral Tian Shan, *Journal of Sedimentary
926 Research*, 70, 520-532, doi:10.1306/2dc40924-0e47-11d7-
927 8643000102c1865d, 2000.

928 Hendrix, M. S., Graham, S. A., Carroll, A. R., Sobel, E. R., McKnight, C. L.,
929 Schulein, B. J., and Wang, Z.: Sedimentary record and climatic implications
930 of recurrent deformation in the Tian Shan: Evidence from Mesozoic strata
931 of the north Tarim, south Junggar, and Turpan basins, northwest China,
932 *GSA Bulletin*, 104, 53-79, 10.1130/0016-
933 7606(1992)104<0053:Srcio>2.3.Co;2, 1992.

934 Hoskin, P. W. O. and Schaltegger, U.: The Composition of Zircon and Igneous
935 and Metamorphic Petrogenesis, *Reviews in Mineralogy and Geochemistry*,
936 53, 27-62, 10.2113/0530027, 2003.

937 Hunziker, D., Burg, J.-P., Bouilhol, P., and von Quadt, A.: Jurassic rifting at the
938 Eurasian Tethys margin: Geochemical and geochronological constraints
939 from granitoids of North Makran, southeastern Iran, *Tectonics*, 34, 571-593,
940 <https://doi.org/10.1002/2014TC003768>, 2015.

941 Hou, Z., Duan, L., Lu, Y., Zheng, Y., Zhu, D., Yang, Z., Yang, Z., Wang, B., Pei,
942 Y., Zhao, Z., and McCuaig, T. C.: Lithospheric Architecture of the Lhasa
943 Terrane and Its Control on Ore Deposits in the Himalayan-Tibetan Orogen*,
944 *Economic Geology*, 110, 1541-1575, 10.2113/econgeo.110.6.1541, 2015.

945 Jafari, A., Ao, S., Jamei, S., and Ghasemi, H.: Evolution of the Zagros sector of
946 Neo-Tethys: Tectonic and magmatic events that shaped its rifting, seafloor

947 spreading and subduction history, *Earth-Science Reviews*, 241, 104419,
948 <https://doi.org/10.1016/j.earscirev.2023.104419>, 2023.

949 Jagoutz, O., Bouilhol, P., Schaltegger, U., and Müntener, O.: The isotopic
950 evolution of the Kohistan Ladakh arc from subduction initiation to continent
951 arc collision, in: *Himalayan Tectonics: A Modern Synthesis*, edited by:
952 Treloar, P. J., and Searle, M. P., The Geological Society of London, 0,
953 10.1144/sp483.7, 2019.

954 Jian, K., Gao, F., Du, B., Zhang, Z., Wang, X., and Zhao, D.: Formation age,
955 geochemical characteristics and tectonic setting of the basalts from
956 Longshan Formation in Heweitan area, Karakorum, *J Mineral Petrol*, 39,
957 42-51, 2019 (in Chinese with English abstract).

958 Jolivet, M.: Mesozoic tectonic and topographic evolution of Central Asia and
959 Tibet: a preliminary synthesis, Geological Society, London, Special
960 Publications, 427, 19-55, doi:10.1144/SP427.2, 2017.

961 Kapp, P. and DeCelles, P. G.: Mesozoic–Cenozoic Geological Evolution of the
962 Himalayan-Tibetan Orogen and Working Tectonic Hypotheses, *American
963 Journal of Science*, 319, 159-+, 10.2475/03.2019.01, 2019.

964 Kapp, P., DeCelles, P. G., Gehrels, G. E., Heizler, M., and Ding, L.: Geological
965 records of the Lhasa-Qiangtang and Indo-Asian collisions in the Nima area
966 of central Tibet, *GSA Bulletin*, 119, 917-933, 10.1130/b26033.1, 2007.

967 Kazmin, V. G.: Collision and rifting in the Tethys Ocean: geodynamic implication,
968 *Tectonophysics*, 196, 371-384, [https://doi.org/10.1016/0040-
969 1951\(91\)90331-L](https://doi.org/10.1016/0040-1951(91)90331-L), 1991.

970 Krienitz, M. S., Haase, K. M., Mezger, K., Eckardt, V., and Shaikh-Mashail, M.
971 A.: Magma genesis and crustal contamination of continental intraplate

972 lavas in northwestern Syria, *Contributions to Mineralogy and Petrology*,
973 151, 698-716, 10.1007/s00410-006-0088-1, 2006.

974 Lechmann, A., Burg, J.-P., Ulmer, P., Mohammadi, A., Guillong, M., and Faridi,
975 M.: From Jurassic rifting to Cretaceous subduction in NW Iranian
976 Azerbaijan: geochronological and geochemical signals from granitoids,
977 *Contributions to Mineralogy and Petrology*, 173, 102, 10.1007/s00410-018-
978 1532-8, 2018.

979 Leith, W.: A mid-Mesozoic extension across Central Asia?, *Nature*, 313, 567-
980 570, 10.1038/313567a0, 1985.

981 Li, G., Sandiford, M., Fang, A., Kohn, B., Sandiford, D., Fu, B., Zhang, T., Cao,
982 Y., and Chen, F.: Multi-stage exhumation history of the West Kunlun orogen
983 and the amalgamation of the Tibetan Plateau, *Earth and Planetary Science*
984 *Letters*, 528, 115833, <https://doi.org/10.1016/j.epsl.2019.115833>, 2019.

985 Li, L., Najman, Y., Dupont-Nivet, G., Parra, M., Roperch, P., Kaya, M., Meijer,
986 N., O'Sullivan, P., Jepson, G., and Aminov, J.: Mesozoic–Cenozoic
987 multistage tectonic evolution of the Pamir: Detrital fission-track constraints
988 from the Tajik Basin, *Basin Research*, 35, 530-550,
989 <https://doi.org/10.1111/bre.12721>, 2023.

990 Li, S., Zhao, S., Liu, X., Cao, H., Yu, S., Li, X., Somerville, I., Yu, S., and Suo,
991 Y.: Closure of the Proto-Tethys Ocean and Early Paleozoic amalgamation
992 of microcontinental blocks in East Asia, *Earth-Science Reviews*, 186, 37-
993 75, <https://doi.org/10.1016/j.earscirev.2017.01.011>, 2018.

994 Li, Y., Robinson, A. C., Zucali, M., Gadoev, M., Oimuhammadzoda, I., Lapen, T.
995 J., and Carrapa, B.: Mesozoic Tectonic Evolution in the Kurgovat-Vanch
996 Complex, NW Pamir, *Tectonics*, 41, e2021TC007180,

997 <https://doi.org/10.1029/2021TC007180>, 2022b.

998 Liao, S., Jiang, Y., Zhou, Q., Yang, W., Jin, G., and Zhao, P.: Geochemistry and
999 geodynamic implications of the Triassic bimodal magmatism from Western
1000 Kunlun Orogen, northwest China, *International Journal of Earth Sciences*,
1001 101, 555-577, [10.1007/s00531-011-0686-7](https://doi.org/10.1007/s00531-011-0686-7), 2012.

1002 Ma, A., Hu, X., Garzanti, E., Han, Z., and Lai, W.: Sedimentary and tectonic
1003 evolution of the southern Qiangtang basin: Implications for the Lhasa-
1004 Qiangtang collision timing, *Journal of Geophysical Research: Solid Earth*,
1005 122, 4790-4813, <https://doi.org/10.1002/2017JB014211>, 2017a.

1006 Ma, A., Hu, X., Kapp, P., Han, Z., Lai, W., and BouDagher-Fadel, M.: The
1007 disappearance of a Late Jurassic remnant sea in the southern Qiangtang
1008 Block (Shamuluo Formation, Najiangco area): Implications for the tectonic
1009 uplift of central Tibet, *Palaeogeography, Palaeoclimatology, Palaeoecology*,
1010 506, 30-47, <https://doi.org/10.1016/j.palaeo.2018.06.005>, 2018.

1011 Ma, S., Wang, Y., and Fang, X.: Basic characteristics of Proterozoic Eonothem
1012 as a table cover on northern slope, *Xinjiang Geology*, 9, 59-71, 1991 (in
1013 Chinese with English abstract).

1014 Ma, X., Xu, Z., Meert, J., and Santosh, M.: Early Jurassic intra-oceanic arc
1015 system of the Neotethys Ocean: Constraints from andesites in the
1016 Gangdese magmatic belt, south Tibet, *Island Arc*, 26, e12202,
1017 <https://doi.org/10.1111/iar.12202>, 2017b.

1018 Maghdour-Mashhour, R., Hayes, B., Pang, K.-N., Bolhar, R., Tabbakh Shabani,
1019 A. A., and Elahi-Janatmakan, F.: Episodic subduction initiation triggered
1020 Jurassic magmatism in the Sanandaj–Sirjan zone, Iran, *Lithos*, 396-397,
1021 106189, <https://doi.org/10.1016/j.lithos.2021.106189>, 2021.

1022 Mattern, F. and Schneider, W.: Suturing of the Proto- and Paleo-Tethys oceans
1023 in the western Kunlun (Xinjiang, China), *Journal of Asian Earth Sciences*,
1024 18, 637-650, [https://doi.org/10.1016/S1367-9120\(00\)00011-0](https://doi.org/10.1016/S1367-9120(00)00011-0), 2000.

1025 Meschede, M.: A method of discriminating between different types of mid-ocean
1026 ridge basalts and continental tholeiites with the Nb 1bZr 1bY diagram,
1027 *Chemical Geology*, 56, 207-218, [https://doi.org/10.1016/0009-](https://doi.org/10.1016/0009-2541(86)90004-5)
1028 2541(86)90004-5, 1986.

1029 Metcalfe, I.: Gondwana dispersion and Asian accretion: Tectonic and
1030 palaeogeographic evolution of eastern Tethys, *Journal of Asian Earth*
1031 *Sciences*, 66, 1-33, 10.1016/j.jseaes.2012.12.020, 2013.

1032 Metcalfe, I.: Multiple Tethyan ocean basins and orogenic belts in Asia,
1033 *Gondwana Research*, 100, 87-130,
1034 <https://doi.org/10.1016/j.gr.2021.01.012>, 2021.

1035 Middlemost, E. A. K.: Naming materials in the magma/igneous rock system,
1036 *Earth-Science Reviews*, 37, 215-224, [https://doi.org/10.1016/0012-](https://doi.org/10.1016/0012-8252(94)90029-9)
1037 8252(94)90029-9, 1994.

1038 Murphy, M. A., Yin, A., Harrison, T. M., Dürr, S. B., Z, C., Ryerson, F. J., Kidd,
1039 W. S. F., X, W., and X, Z.: Did the Indo-Asian collision alone create the
1040 Tibetan plateau?, *Geology*, 25, 719-722, 10.1130/0091-
1041 7613(1997)025<0719:Dtiaca>2.3.Co;2, 1997.

1042 Otto, S. C.: Mesozoic-Cenozoic history of deformation and petroleum systems
1043 in sedimentary basins of Central Asia; implications of collisions on the
1044 Eurasian margin, *Petroleum Geoscience*, 3, 327-341,
1045 10.1144/petgeo.3.4.327, 1997.

1046 Pearce, J. A.: Geochemical fingerprinting of oceanic basalts with applications

1047 to ophiolite classification and the search for Archean oceanic crust, *Lithos*,
1048 100, 14-48, <https://doi.org/10.1016/j.lithos.2007.06.016>, 2008.

1049 Pearce, J. A.: Trace element characteristics of lavas from destructive plate
1050 boundaries, in: *Orogenic Andesites and Related Rocks*, edited by: Thorpe,
1051 R. S., John Wiley and Sons, Chichester, England, 525-548, 1982.

1052 Qu, J., Zhang, L., Zhang, J., and Zhang, B.: Petrology and geochronology on
1053 high-pressure pelitic granulite from Bulunkuole complex in West Kunlun
1054 and its tectonic implication, *Acta Petrologica Siniaca*, 37, 563-574,
1055 [10.18654/1000-0569/2021.02.14](https://doi.org/10.18654/1000-0569/2021.02.14), 2021.

1056 Rembe, J., Sobel, E. R., Kley, J., Terbishaliev, B., Musiol, A., Chen, J., and
1057 Zhou, R.: Geochronology, Geochemistry, and Geodynamic Implications of
1058 Permo-Triassic Back-Arc Basin Successions in the North Pamir, Central
1059 Asia, *Lithosphere*, 2022, [10.2113/2022/7514691](https://doi.org/10.2113/2022/7514691), 2022.

1060 Robinson, A. C.: Mesozoic tectonics of the Gondwanan terranes of the Pamir
1061 plateau, *Journal of Asian Earth Sciences*, 102, 170-179,
1062 <https://doi.org/10.1016/j.jseaes.2014.09.012>, 2015.

1063 Robinson, A. C., Yin, A., Manning, C. E., Harrison, T. M., Zhang, S.-H., and
1064 Wang, X.-F.: Cenozoic evolution of the eastern Pamir: Implications for
1065 strain-accommodation mechanisms at the western end of the Himalayan-
1066 Tibetan orogen, *GSA Bulletin*, 119, 882-896, [10.1130/b25981.1](https://doi.org/10.1130/b25981.1), 2007.

1067 Rollinson, H. R.: *Using Geochemical Data: Evaluation, Presentation,*
1068 *Interpretation*, Mineralogical Magazine, Longman, Edinburgh Gate,
1069 London, 352 pp.1993.

1070 Ruban, D. A., Al-Husseini, M. I., and Iwasaki, Y.: Review of Middle East
1071 Paleozoic plate tectonics, *GeoArabia*, 12, 35-56,

1072 10.2113/geoarabia120335, 2007.

1073 Saktura, W. M., Buckman, S., Nutman, A. P., Walsh, J., and Murray, G.:
1074 Magmatic records from the Karakoram terrane: U–Pb zircon ages from
1075 granites and modern sediments in the Nubra Valley, NW Himalaya, Journal
1076 of Asian Earth Sciences, 255, 105771,
1077 <https://doi.org/10.1016/j.jseaes.2023.105771>, 2023.

1078 Schwab, M., Ratschbacher, L., Siebel, W., McWilliams, M., Minaev, V., Lutkov,
1079 V., Chen, F., Stanek, K., Nelson, B., Frisch, W., and Wooden, J. L.:
1080 Assembly of the Pamirs: Age and origin of magmatic belts from the
1081 southern Tien Shan to the southern Pamirs and their relation to Tibet,
1082 Tectonics, 23, <https://doi.org/10.1029/2003TC001583>, 2004.

1083 Şengör, A. M. C.: Mid-Mesozoic closure of Permo–Triassic Tethys and its
1084 implications, Nature, 279, 590-593, 10.1038/279590a0, 1979.

1085 Şengör, A. M. C.: The Cimmeride Orogenic System and the Tectonics of
1086 Eurasia, in: The Cimmeride Orogenic System and the Tectonics of Eurasia,
1087 Geological Society of America, 0, 10.1130/SPE195-p1, 1984.

1088 Şengör, A. M. C.: Tectonics of the Tethysides: Orogenic Collage Development
1089 in a Collisional Setting, Annual Review of Earth and Planetary Sciences,
1090 15, 213-244, <https://doi.org/10.1146/annurev.ea.15.050187.001241>, 1987.

1091 Şengör, A. M. C., Altiner, D., Cin, A., Ustaömer, T., and Hsü, K. J.: Origin and
1092 assembly of the Tethyside orogenic collage at the expense of Gondwana
1093 Land, Geological Society, London, Special Publications, 37, 119-181,
1094 doi:10.1144/GSL.SP.1988.037.01.09, 1988.

1095 Sobel, E. R.: Basin analysis of the Jurassic–Lower Cretaceous southwest Tarim
1096 basin, northwest China, GSA Bulletin, 111, 709-724, 10.1130/0016-

1097 7606(1999)111<0709:Baotjl>2.3.Co;2, 1999.

1098 Sobel, E. R., Chen, J., Schoenbohm, L. M., Thiede, R., Stockli, D. F., Sudo, M.,
1099 and Strecker, M. R.: Oceanic-style subduction controls late Cenozoic
1100 deformation of the Northern Pamir orogen, *Earth and Planetary Science*
1101 *Letters*, 363, 204-218, <https://doi.org/10.1016/j.epsl.2012.12.009>, 2013.

1102 Stampfli, G., Marcoux, J., and Baud, A.: Tethyan margins in space and time,
1103 *Palaeogeography, Palaeoclimatology, Palaeoecology*, 87, 373-409,
1104 [https://doi.org/10.1016/0031-0182\(91\)90142-E](https://doi.org/10.1016/0031-0182(91)90142-E), 1991.

1105 Stampfli, G. M.: Tethyan oceans, Geological Society, London, Special
1106 Publications, 173, 1-23, doi:10.1144/GSL.SP.2000.173.01.01, 2000.

1107 Stampfli, G. M. and Borel, G. D.: A plate tectonic model for the Paleozoic and
1108 Mesozoic constrained by dynamic plate boundaries and restored synthetic
1109 oceanic isochrons, *Earth and Planetary Science Letters*, 196, 17-33,
1110 [https://doi.org/10.1016/S0012-821X\(01\)00588-X](https://doi.org/10.1016/S0012-821X(01)00588-X), 2002.

1111 Sun, S.-S. and McDonough, W. F.: Chemical and isotopic systematics of
1112 oceanic basalts: implications for mantle composition and processes,
1113 Geological Society, London, Special Publications, 42, 313-345,
1114 doi:10.1144/GSL.SP.1989.042.01.19, 1989.

1115 Tapponnier, P., Mattauer, M., Proust, F., and Cassaigneau, C.: Mesozoic
1116 ophiolites, sutures, and large-scale tectonic movements in Afghanistan,
1117 *Earth and Planetary Science Letters*, 52, 355-371,
1118 [https://doi.org/10.1016/0012-821X\(81\)90189-8](https://doi.org/10.1016/0012-821X(81)90189-8), 1981.

1119 Tao, Z., Yin, J., Spencer, C. J., Sun, M., Xiao, W., Kerr, A. C., Wang, T., Huangfu,
1120 P., Zeng, Y., and Chen, W.: Subduction polarity reversal facilitated by plate
1121 coupling during arc-continent collision: Evidence from the Western Kunlun

1122 orogenic belt, northwest Tibetan Plateau, *Geology*, 10.1130/g51847.1,
1123 2024.

1124 Vermeesch, P.: IsoplotR: A free and open toolbox for geochronology,
1125 *Geoscience Frontiers*, 9, 1479-1493,
1126 <https://doi.org/10.1016/j.gsf.2018.04.001>, 2018.

1127 Vermeesch, P.: On the visualisation of detrital age distributions, *Chemical*
1128 *Geology*, 312-313, 190-194,
1129 <https://doi.org/10.1016/j.chemgeo.2012.04.021>, 2012.

1130 Wan, B., Chu, Y., Chen, L., Zhang, Z., Ao, S., and Talebian, M.: When and Why
1131 the NeoTethyan Subduction Initiated Along the Eurasian Margin, in:
1132 *Compressional Tectonics*, 245-260,
1133 <https://doi.org/10.1002/9781119773856.ch9>, 2023.

1134 Wan, B., Wu, F., Chen, L., Zhao, L., Liang, X., Xiao, W., and Zhu, R.: Cyclical
1135 one-way continental rupture-drift in the Tethyan evolution: Subduction-
1136 driven plate tectonics, *Science China Earth Sciences*, 62, 2005-2016,
1137 10.1007/s11430-019-9393-4, 2019.

1138 Wang, C., Ding, L., Zhang, L.-Y., Kapp, P., Pullen, A., and Yue, Y.-H.:
1139 Petrogenesis of Middle–Late Triassic volcanic rocks from the Gangdese
1140 belt, southern Lhasa terrane: Implications for early subduction of Neo-
1141 Tethyan oceanic lithosphere, *Lithos*, 262, 320-333,
1142 <https://doi.org/10.1016/j.lithos.2016.07.021>, 2016.

1143 Wang, Y., Qian, X., Cawood, P. A., Liu, H., Feng, Q., Zhao, G., Zhang, Y., He,
1144 H., and Zhang, P.: Closure of the East Paleotethyan Ocean and
1145 amalgamation of the Eastern Cimmerian and Southeast Asia continental
1146 fragments, *Earth-Science Reviews*, 186, 195-230,

1147 <https://doi.org/10.1016/j.earscirev.2017.09.013>, 2018.

1148 Wei, Y., Zhao, Z., Niu, Y., Zhu, D.-C., Liu, D., Wang, Q., Hou, Z., Mo, X., and
1149 Wei, J.: Geochronology and geochemistry of the Early Jurassic Yeba
1150 Formation volcanic rocks in southern Tibet: Initiation of back-arc rifting and
1151 crustal accretion in the southern Lhasa Terrane, *Lithos*, 278-281, 477-490,
1152 <https://doi.org/10.1016/j.lithos.2017.02.013>, 2017.

1153 Weller, O. M., Mottram, C. M., St-Onge, M. R., Möller, C., Strachan, R., Rivers,
1154 T., and Copley, A.: The metamorphic and magmatic record of collisional
1155 orogens, *Nature Reviews Earth & Environment*, 2, 781-799,
1156 [10.1038/s43017-021-00218-z](https://doi.org/10.1038/s43017-021-00218-z), 2021.

1157 Winchester, J. A. and Floyd, P. A.: Geochemical discrimination of different
1158 magma series and their differentiation products using immobile elements,
1159 *Chemical Geology*, 20, 325-343, [https://doi.org/10.1016/0009-](https://doi.org/10.1016/0009-2541(77)90057-2)
1160 [2541\(77\)90057-2](https://doi.org/10.1016/0009-2541(77)90057-2), 1977.

1161 Wu, C., Yin, A., Zuba, A. V., Zhang, J., Liu, W., and Ding, L.: Pre-Cenozoic
1162 geologic history of the central and northern Tibetan Plateau and the role of
1163 Wilson cycles in constructing the Tethyan orogenic system, *Lithosphere*, 8,
1164 254-292, [10.1130/l494.1](https://doi.org/10.1130/l494.1), 2016.

1165 Wu, F. Y., Wan, B., Zhao, L., Xiao, W. J., and Zhu, R. X.: Tethyan geodynamics,
1166 *Acta Petrologica Siniaca*, 36, 1627-1674, 2020.

1167 Wu, H., Cheng, X., Chen, H., Chen, C., Dilek, Y., Shi, J., Zeng, C., Li, C., Zhang,
1168 W., Zhang, Y., Lin, X., and Zhang, F.: Tectonic Switch From Triassic
1169 Contraction to Jurassic-Cretaceous Extension in the Western Tarim Basin,
1170 Northwest China: New Insights Into the Evolution of the Paleo-Tethyan
1171 Orogenic Belt, *Frontiers in Earth Science*, 9, [10.3389/feart.2021.636383](https://doi.org/10.3389/feart.2021.636383),

1172 2021.

1173 Xia, Y., Yang, X., Hu, C., Lin, H., and Li, H.: Sedimentary infill of Early-Middle
1174 Jurassic in the southeastern Tarim Basin and its constraints on the
1175 evolution of the Altyn Tagh Fault in the Northeast Tibet Plateau, *Marine and*
1176 *Petroleum Geology*, 161, 106657,
1177 <https://doi.org/10.1016/j.marpetgeo.2023.106657>, 2024.

1178 Xiao, W. J., Windley, B. F., Chen, H. L., Zhang, G. C., and Li, J. L.:
1179 Carboniferous-Triassic subduction and accretion in the western Kunlun,
1180 China: Implications for the collisional and accretionary tectonics of the
1181 northern Tibetan Plateau, *Geology*, 30, 295-298, 10.1130/0091-
1182 7613(2002)030<0295:Ctsaai>2.0.Co;2, 2002.

1183 Xiao, W. J., Windley, B. F., Liu, D. Y., Jian, P., Liu, C. Z., Yuan, C., and Sun, M.:
1184 Accretionary Tectonics of the Western Kunlun Orogen, China: A Paleozoic–
1185 Early Mesozoic, Long - Lived Active Continental Margin with Implications
1186 for the Growth of Southern Eurasia, *The Journal of Geology*, 113, 687-705,
1187 [10.1086/449326](https://doi.org/10.1086/449326), 2005.

1188 Xie, F. and Tang, J.: The Late Triassic-Jurassic magmatic belt and its
1189 implications for the double subduction of the Neo-Tethys Ocean in the
1190 southern Lhasa subterrane, Tibet, *Gondwana Research*, 97, 1-21,
1191 <https://doi.org/10.1016/j.gr.2021.05.007>, 2021.

1192 Xie, Y. and Dilek, Y.: Detrital zircon U–Pb geochronology and fluvial basin
1193 evolution of the Liuqu Conglomerate within the Yarlung Zangbo Suture
1194 Zone: A critical geochronometer for the collision tectonics of the Tibetan-
1195 Himalayan Orogenic Belt, *Geosystems and Geoenvironment*, 2, 100178,
1196 <https://doi.org/10.1016/j.geogeo.2023.100178>, 2023.

1197 Yan, J.: The early Paleozoic tectono-sedimentary characteristics and the basin-
1198 orogen process in south Tarim Basin, School of Earth Sciences, Zhejiang
1199 University, Hangzhou, Zhejiang, China, 137 pp.,
1200 10.27461/d.cnki.gzjdx.2022.002783, 2022 (in Chinese with English
1201 abstract).

1202 Yang, Y.-T., Guo, Z.-X., and Luo, Y.-J.: Middle-Late Jurassic
1203 tectonostratigraphic evolution of Central Asia, implications for the collision
1204 of the Karakoram-Lhasa Block with Asia, *Earth-Science Reviews*, 166, 83-
1205 110, <https://doi.org/10.1016/j.earscirev.2017.01.005>, 2017.

1206 Zhang, K.-J., Zhang, Y.-X., Tang, X.-C., and Xia, B.: Late Mesozoic tectonic
1207 evolution and growth of the Tibetan plateau prior to the Indo-Asian collision,
1208 *Earth-Science Reviews*, 114, 236-249,
1209 <https://doi.org/10.1016/j.earscirev.2012.06.001>, 2012.

1210 Zhang, Q., Wu, Z., Chen, X., Zhou, Q., and Shen, N.: Proto-Tethys oceanic slab
1211 break-off: Insights from early Paleozoic magmatic diversity in the West
1212 Kunlun Orogen, NW Tibetan Plateau, *Lithos*, 346-347, 105147,
1213 <https://doi.org/10.1016/j.lithos.2019.07.014>, 2019a.

1214 Zhang, S., Hu, X., and Garzanti, E.: Paleocene initial indentation and early
1215 growth of the Pamir as recorded in the western Tarim Basin,
1216 *Tectonophysics*, 772, 228207, <https://doi.org/10.1016/j.tecto.2019.228207>,
1217 2019b.

1218 Zhang, Z., Xiao, W., Ji, W., Majidifard, M. R., Rezaeian, M., Talebian, M., Xiang,
1219 D., Chen, L., Wan, B., Ao, S., and Esmaeili, R.: Geochemistry, zircon U-Pb
1220 and Hf isotope for granitoids, NW Sanandaj-Sirjan zone, Iran: Implications
1221 for Mesozoic-Cenozoic episodic magmatism during Neo-Tethyan

1222 lithospheric subduction, *Gondwana Research*, 62, 227-245,
1223 <https://doi.org/10.1016/j.gr.2018.04.002>, 2018.

1224 Zhao, G., Wang, Y., Huang, B., Dong, Y., Li, S., Zhang, G., and Yu, S.:
1225 Geological reconstructions of the East Asian blocks: From the breakup of
1226 Rodinia to the assembly of Pangea, *Earth-Science Reviews*, 186, 262-286,
1227 <https://doi.org/10.1016/j.earscirev.2018.10.003>, 2018.

1228 Zhao, X., Zhao, J., Zeng, X., Tian, J., Guo, Z., Wang, C., Wang, D., and Hu, C.:
1229 Early–Middle Jurassic paleogeography reconstruction in the Western
1230 Qaidam Basin: Insights from sedimentology and detrital zircon
1231 geochronology, *Marine and Petroleum Geology*, 118, 104445,
1232 <https://doi.org/10.1016/j.marpetgeo.2020.104445>, 2020.

1233 Zheng, Y., Mao, J., Chen, Y., Sun, W., Ni, P., and Yang, X.: Hydrothermal ore
1234 deposits in collisional orogens, *Science Bulletin*, 64, 205-212,
1235 <https://doi.org/10.1016/j.scib.2019.01.007>, 2019.

1236 Zhou, C.-A., Song, S., Allen, M. B., Wang, C., Su, L., and Wang, M.: Post-
1237 collisional mafic magmatism: Insights into orogenic collapse and mantle
1238 modification from North Qaidam collisional belt, NW China, *Lithos*, 398-
1239 399, 106311, <https://doi.org/10.1016/j.lithos.2021.106311>, 2021.

1240 Zhou, N., Chen, B., Deng, Z., Sang, M., and Bai, Q.: Discovery and Significance
1241 of Early Jurassic Bimodal Volcanic Rocks in Huoshaoyun, Karakoram,
1242 *Geoscience*, 33, 990-1002, [10.19657/j.geoscience.1000-8527.2019.05.06](https://doi.org/10.19657/j.geoscience.1000-8527.2019.05.06),
1243 2019 (in Chinese with English abstract).

1244 Zhu, D.-C., Wang, Q., Cawood, P. A., Zhao, Z.-D., and Mo, X.-X.: Raising the
1245 Gangdese Mountains in southern Tibet, *Journal of Geophysical Research:*
1246 *Solid Earth*, 122, 214-223, <https://doi.org/10.1002/2016JB013508>, 2017.

1247 Zhu, R., Zhao, P., and Zhao, L.: Tectonic evolution and geodynamics of the
1248 Neo-Tethys Ocean, *Science China Earth Sciences*, 65, 1-24,
1249 10.1007/s11430-021-9845-7, 2022.

1250 Zuza, A. V. and Yin, A.: Balkatach hypothesis: A new model for the evolution of
1251 the Pacific, Tethyan, and Paleo-Asian oceanic domains, *Geosphere*, 13,
1252 1664-1712, 10.1130/ges01463.1, 2017.

1253

1254 **Supplementary Materials**

1255 Table S1: Analytical methodology.

1256 Table S2: Zircon U-Pb data of Jurassic basalt and sedimentary rocks.

1257 Table S3: Trace element of zircons.

1258 Table S4: Whole rock geochemical results of Jurassic basalts.

1259 Table S5: Jurassic conglomerate clast lithologies.

1260 Fig. S1: Correlations between the trace elements of Jurassic basalts.

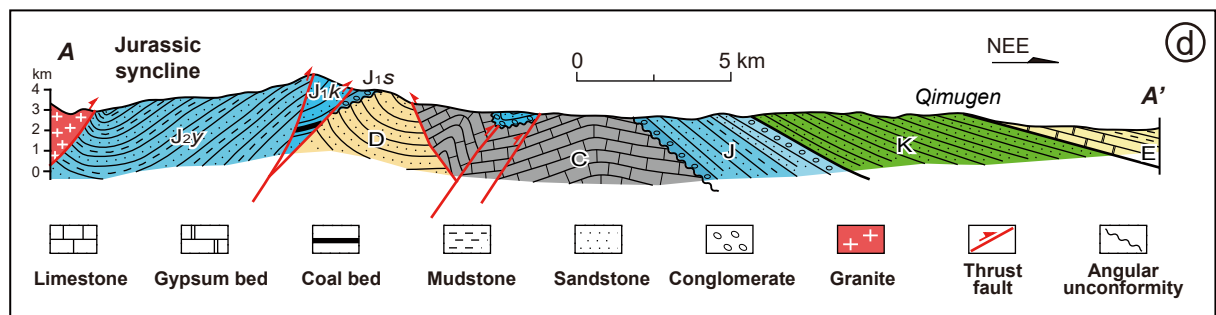
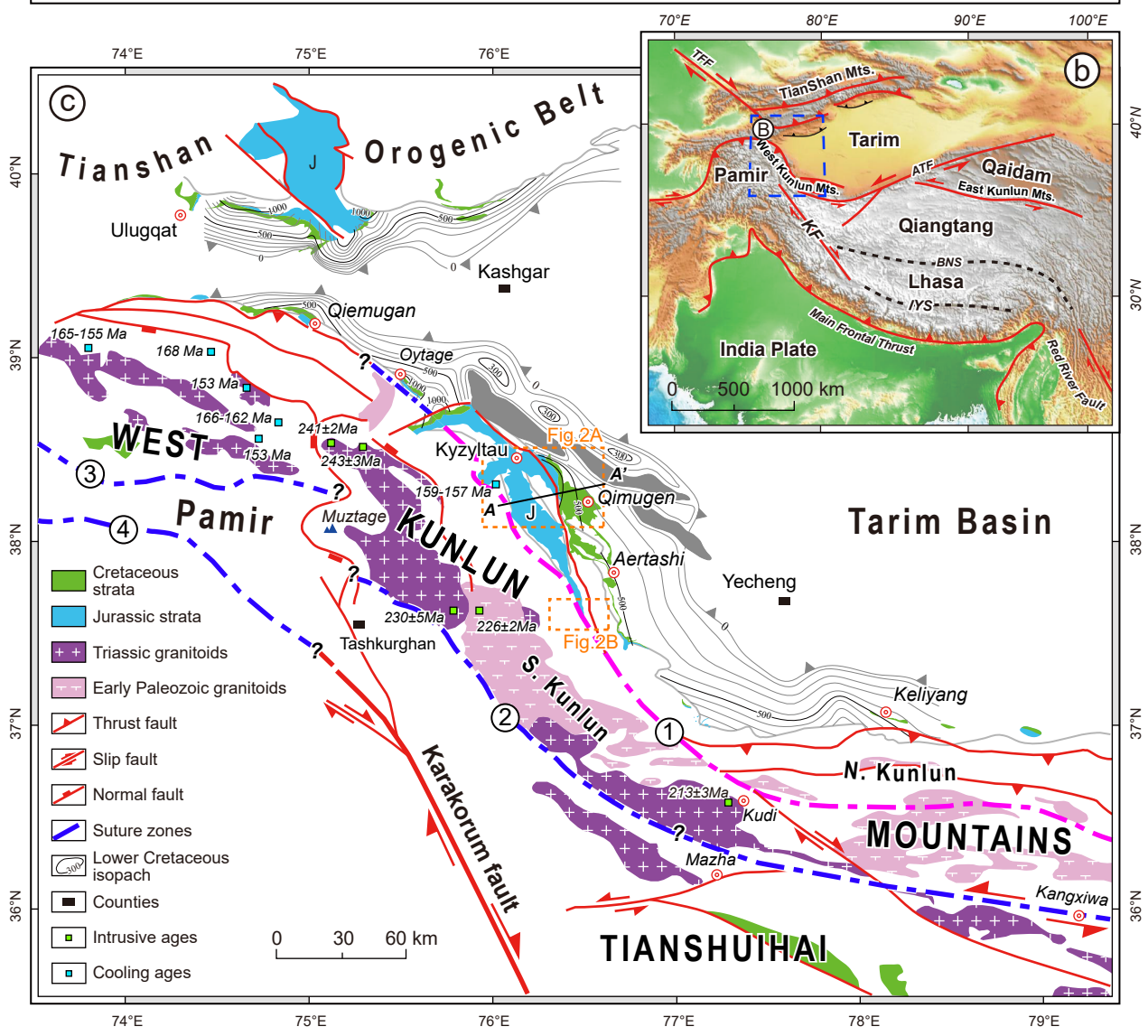
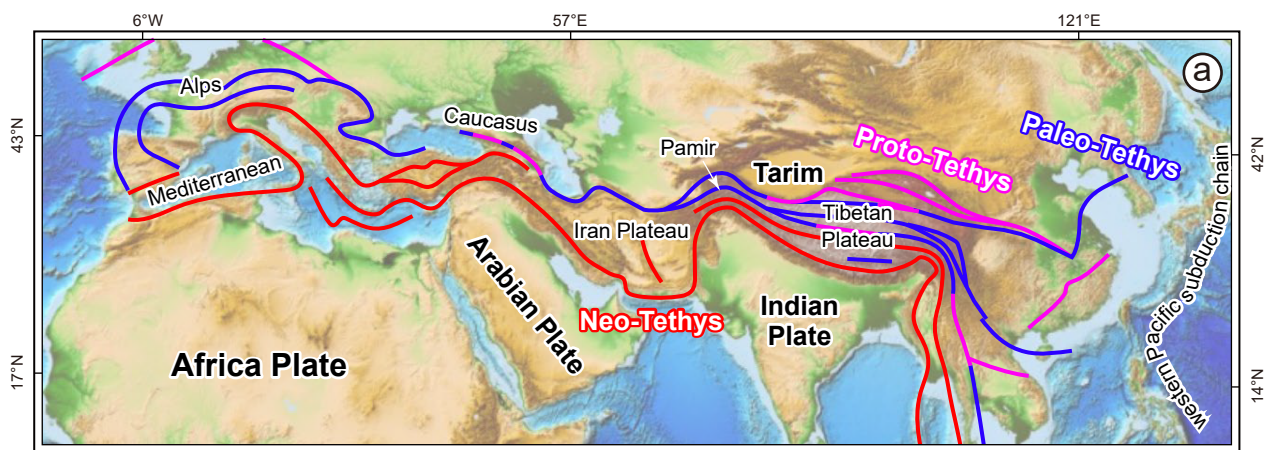


Figure 1 (a) Tectonic plate framework in the Northern Hemisphere and the suture zones within the Tethyan Realm (modified from Wu et al., 2020); (b) Structural framework of central Asia showing main blocks and orogenic belts, with locations of major sutures and boundary faults: TFF-Talas-Fergana Fault, BNS-Bangong-Nujiang suture, IYS-Indus-Yalu suture, ATF-Altyn-Tage Fault; (c) Simplified geologic map of the Western Kunlun Mountains including major units and suture zones (modified from Wu et al., 2021; cooling ages of basements refer to Yang et al., 2017): ①- Early Paleozoic Kudi suture, ②- Triassic Mazar-Kangxiwa suture, ③- Triassic Tanymas suture separating the North and Central Pamirs, ④- Rushan-Pshart zone separating the Central and South Pamirs; (d) A section across the east part of the Western Kunlun Mountains showing the deformed and fragmented Jurassic basin. The section location is presented in Fig.1 (c).

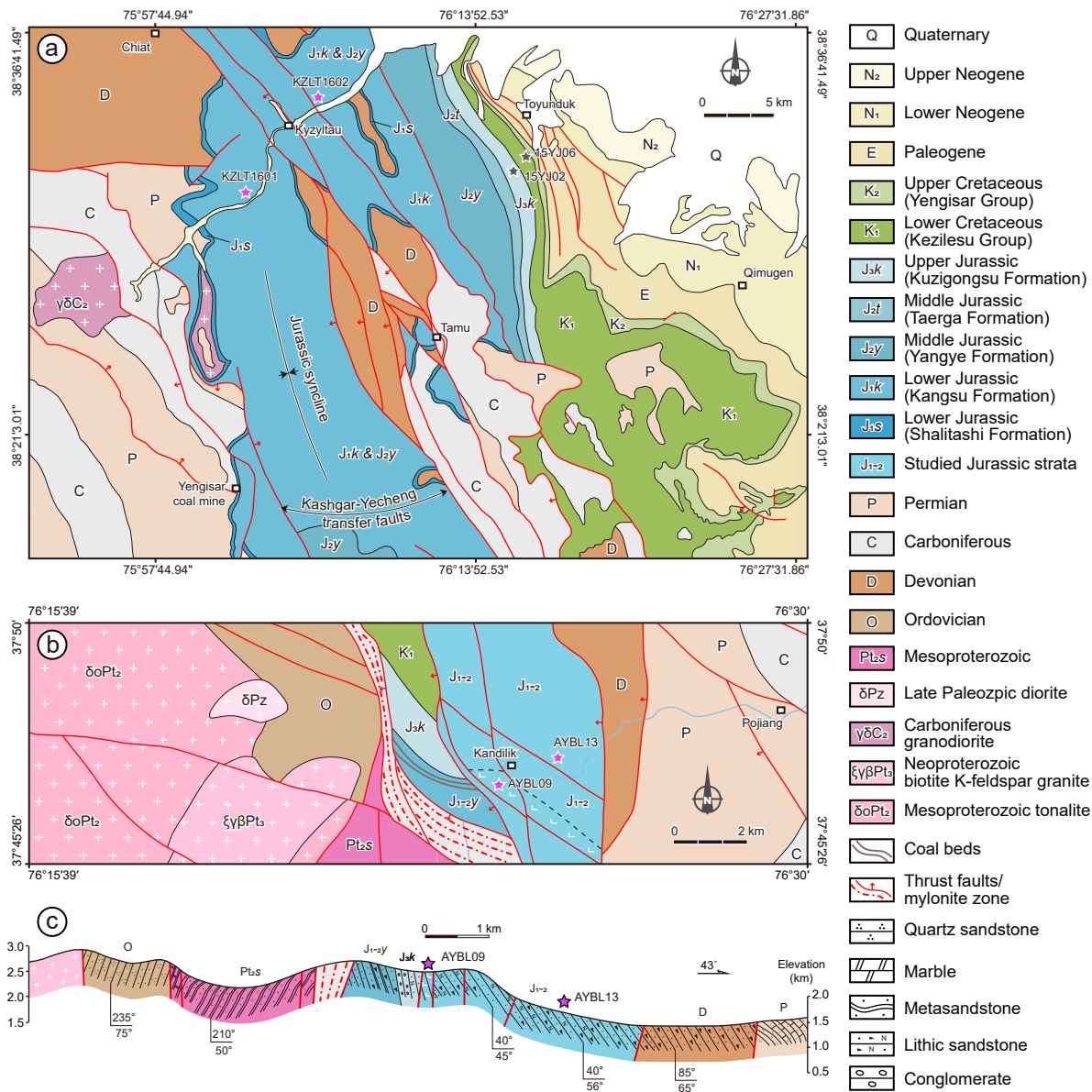


Figure 2 (a) Geological map in the Kyzyltau region showing the stratigraphic information and sampling locations; (b) Geological map in the Kandilik region showing the Proterozoic basements and Paleozoic-Mesozoic strata. The red stars mark sampling locations in this work, and the grey stars mark the locations of published data (Zhang et al., 2019b); (c) A field geological section showing the regional strata and deformation along the Pojiang River in Fig. 2b.

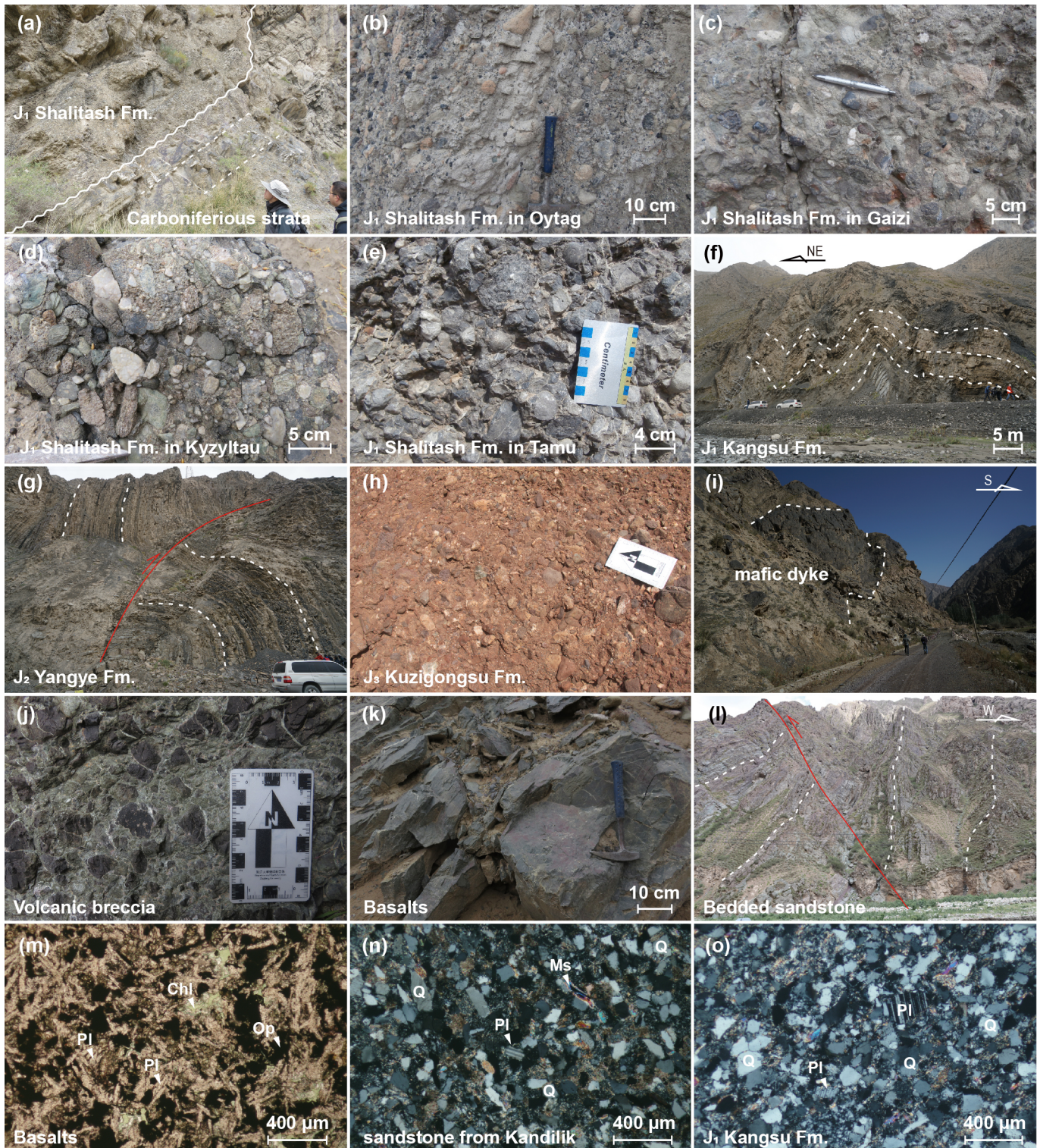


Figure 3 Photographs showing the observation from field and binocular microscope. (a) Early Jurassic Shalitash Formation overlying on the deformed Carboniferous strata with angular unconformity; (b) Conglomerate clast lithologies of the Shalitash Formation in Oytag, (c) Gaizi; (d) Kyzyltau and (e) Tamu; (f) Early Jurassic Kangsu Formation with strongly deformed sandstone layers; (g) Strong deformation of the turbidite sequences in the Middle Jurassic Yangye Formation; (h) Conglomerate clast lithologies in the Late Jurassic Kuzigongsu Formation; (i) Mafic dyke within newly identified Jurassic strata in the Kandilik region; (j) Basaltic volcanic breccia; (k) Massive basalt layer; (l) Jurassic bedded feldspar lithic sandstones with great thickness, which was previously assigned to be Precambrian age; (m) Micrograph of basalt under plane-polarized light; (n) Micrograph of Jurassic sandstone under cross-polarized light from Kandilik section; (o) Micrograph of Jurassic sandstone under cross-polarized light from Kyzyltau section. Abbreviation: Pl-plagioclase; Chl-chlorite; Op-Opaque mineral (mainly Ti-Fe oxides); Q-Quartz.

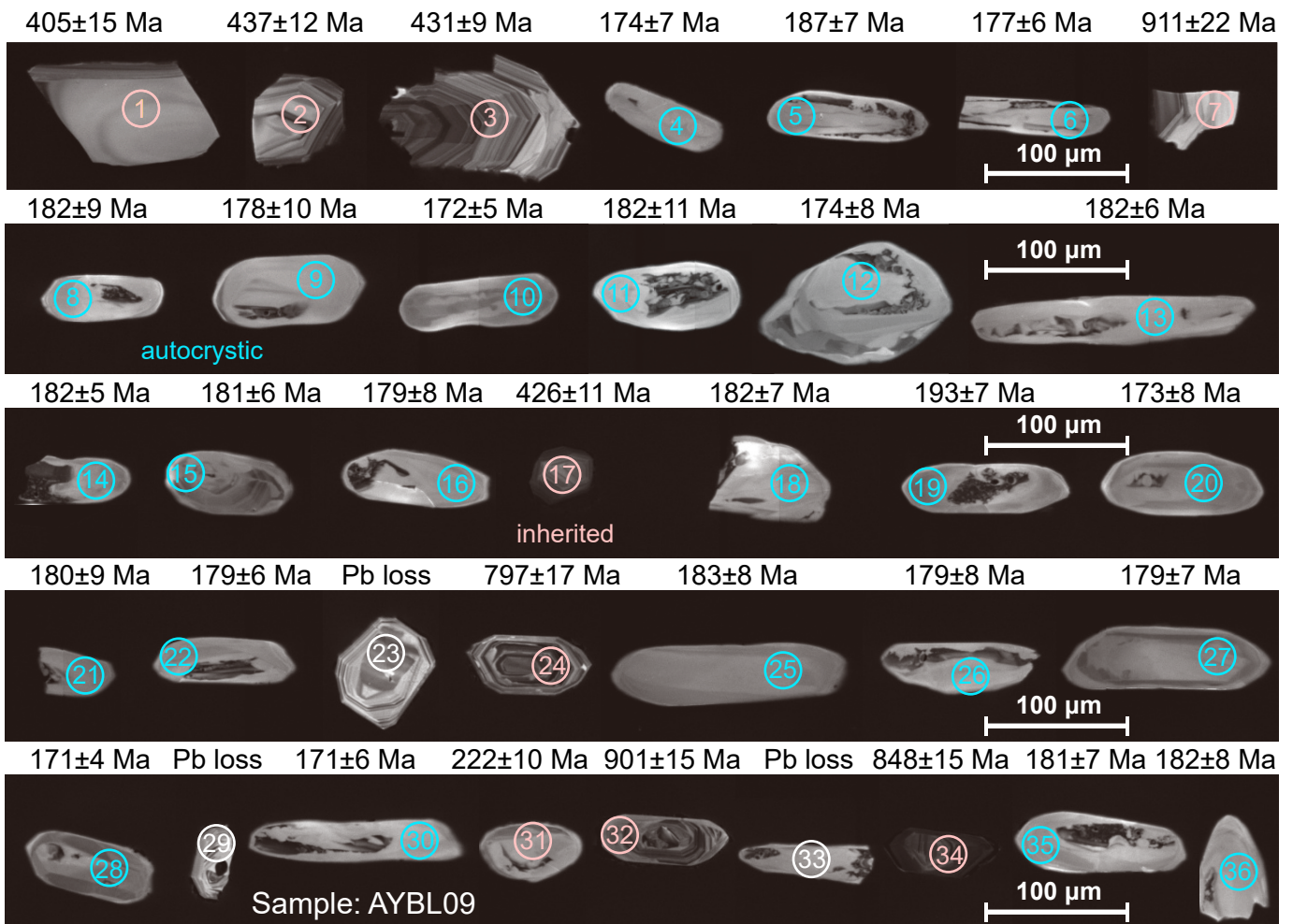


Figure 4 CL images of all tested zircon varieties in basalt sample AYBL09, noting the apparent $^{206}\text{Pb}/^{238}\text{U}$ ages above. The red circle indicates the target points of type 1 zircon, the blue circle represents the target points of type 2 zircon, and the white circle marks the points where discordant ages were obtained.

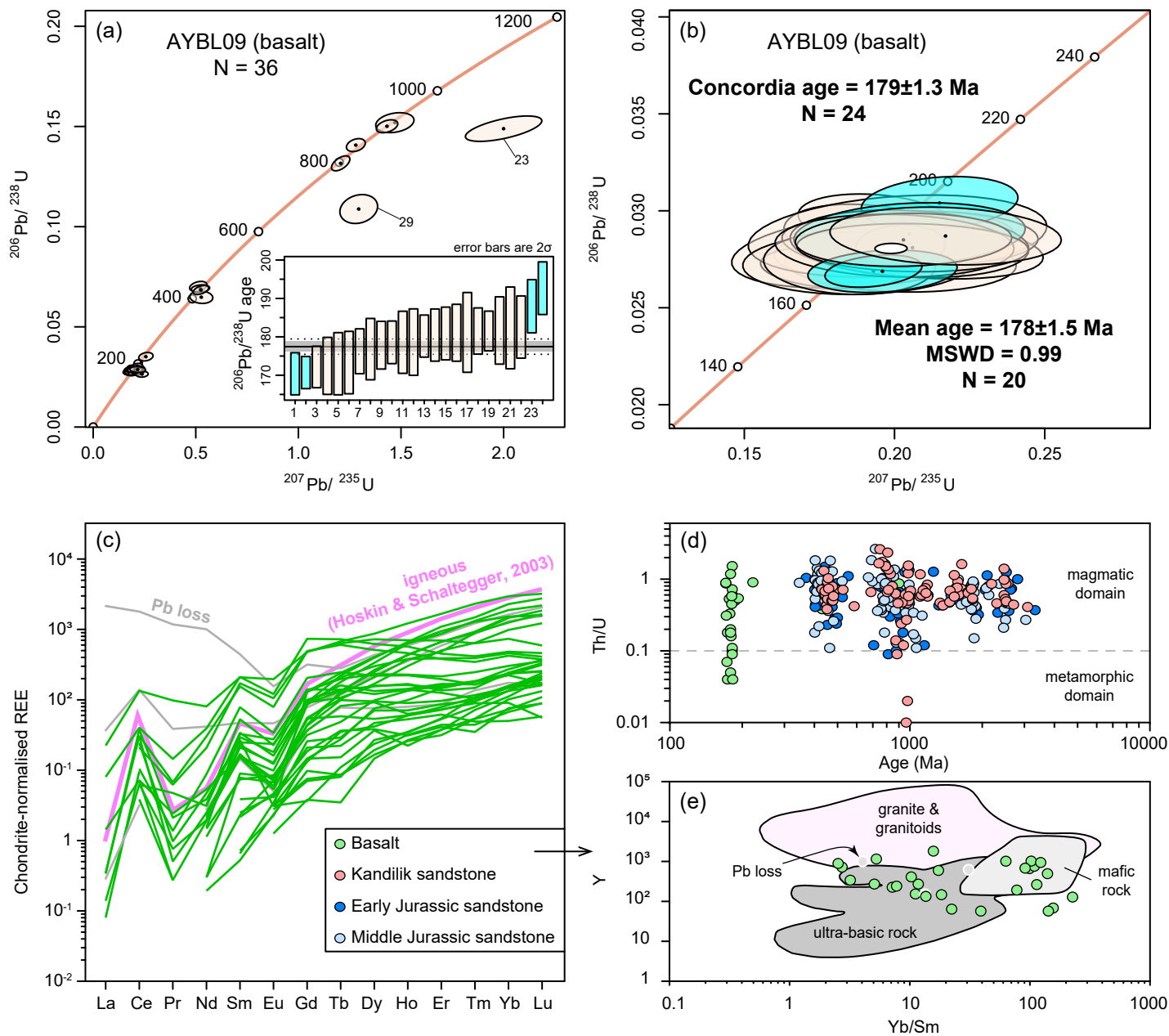


Figure 5 (a) Concordia plot of LA-ICP-MS U-Pb analysis for the zircons of the basalt sample AYBL09; (b) Weighted mean $^{206}\text{Pb}/^{238}\text{U}$ age and concordia age of the youngest zircon groups; (c) Zircon chondrite-normalised REE pattern of the basalt; (d) Th/U ratios of zircons from basalt and sandstone samples. (e) Yb/Sm-Y plotting to distinguish the origins of zircons from the basalt.

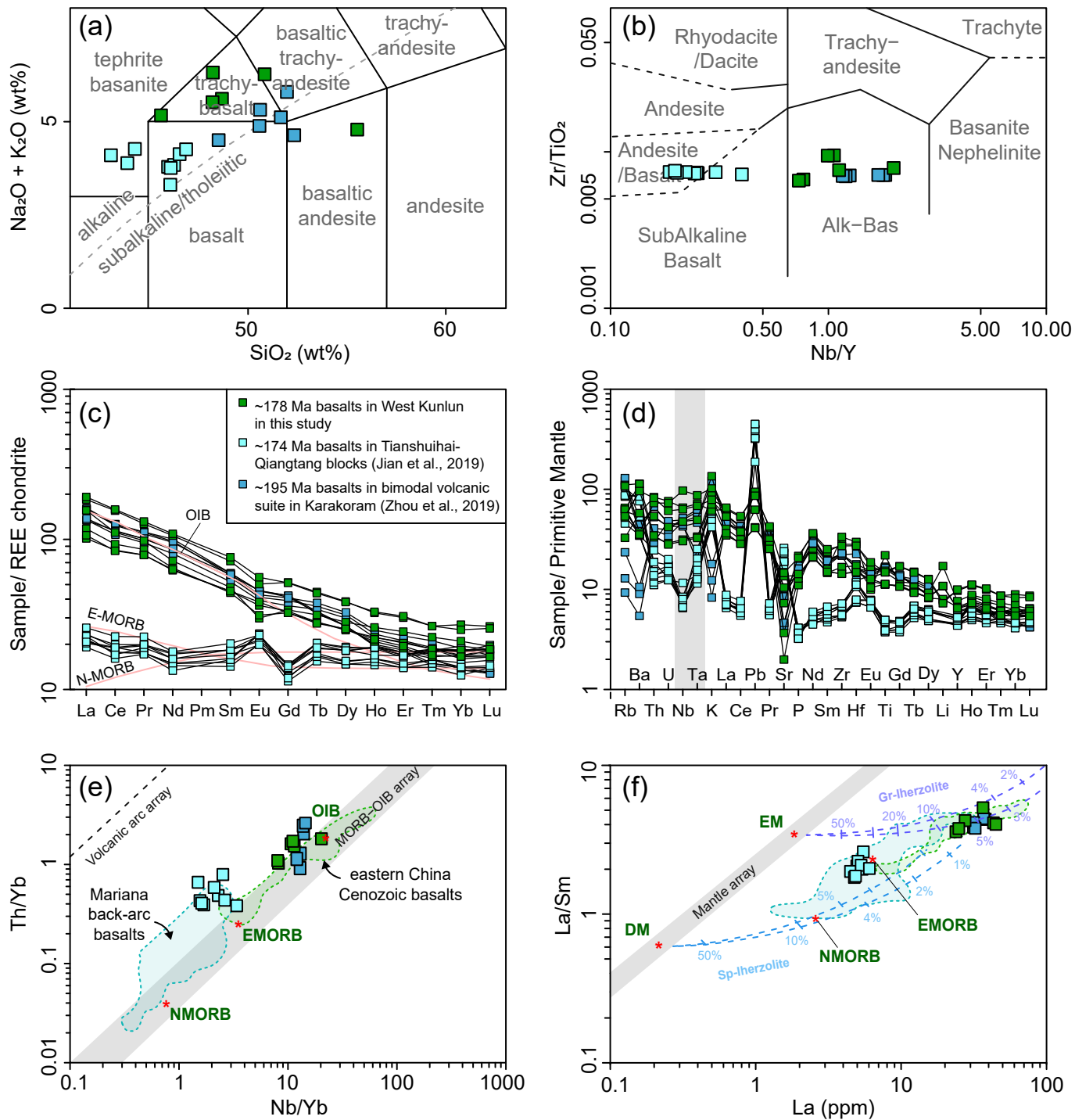


Figure 6 Geochemical classification diagram of Jurassic basalt samples from the Kandilik region in the West Kunlun Mountains (green) and from Longshan Formation in the Tianshuihai terrane (blue): (a) total alkali versus silica (Middlemost, 1994) and (b) Zr/TiO_2 vs. Nb/Y diagrams (Winchester and Floyd, 1977); (c) Rare earth elements pattern (REE) and (d) trace element diagrams of Jurassic basalts; (e) Th/Yb vs. Nb/Yb plot (Pearce, 2008) and (f) La/Sm vs. La plot (Aldanmaz et al., 2000) Chondrite-normalized REE and the primitive mantle-normalized values refer to Sun and McDonough (1989). The range of the Mariana back-arc basalts refers to Pearce (2008) and the range of eastern China Cenozoic basalts refers to Guo et al. (2020).

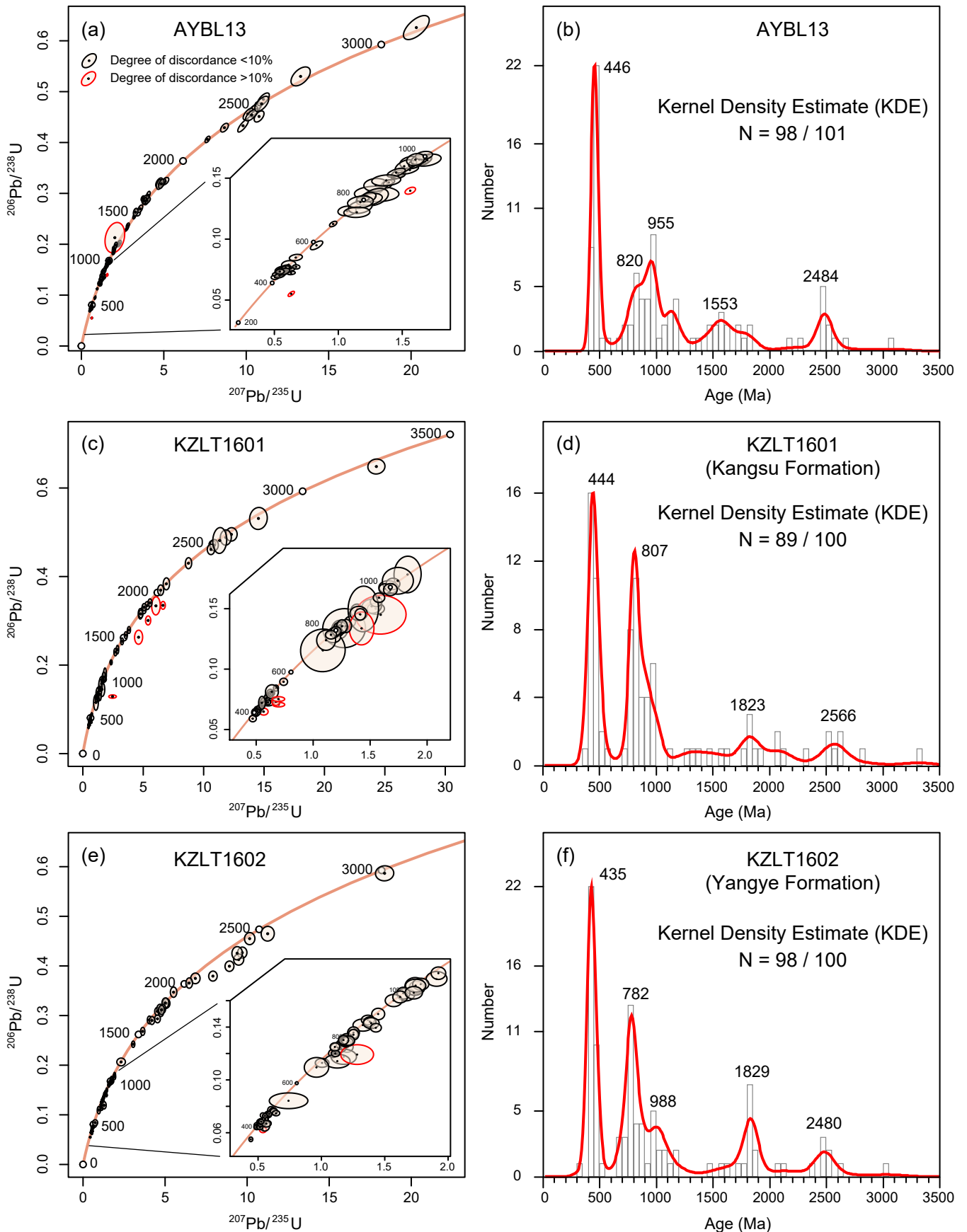


Figure 7 Concordia diagram for the detrital zircons of (a) sample AYBL13 from Kandilik section, (c) sample KZLT1601 from Kangsu Formation, and (e) sample KZLT1602 from Yangye Formation; Diagram of the Kernel Density Estimate of detrital zircon U-Pb ages for (b) AYBL13, (d) KZLT1601, and (f) KZLT1602.

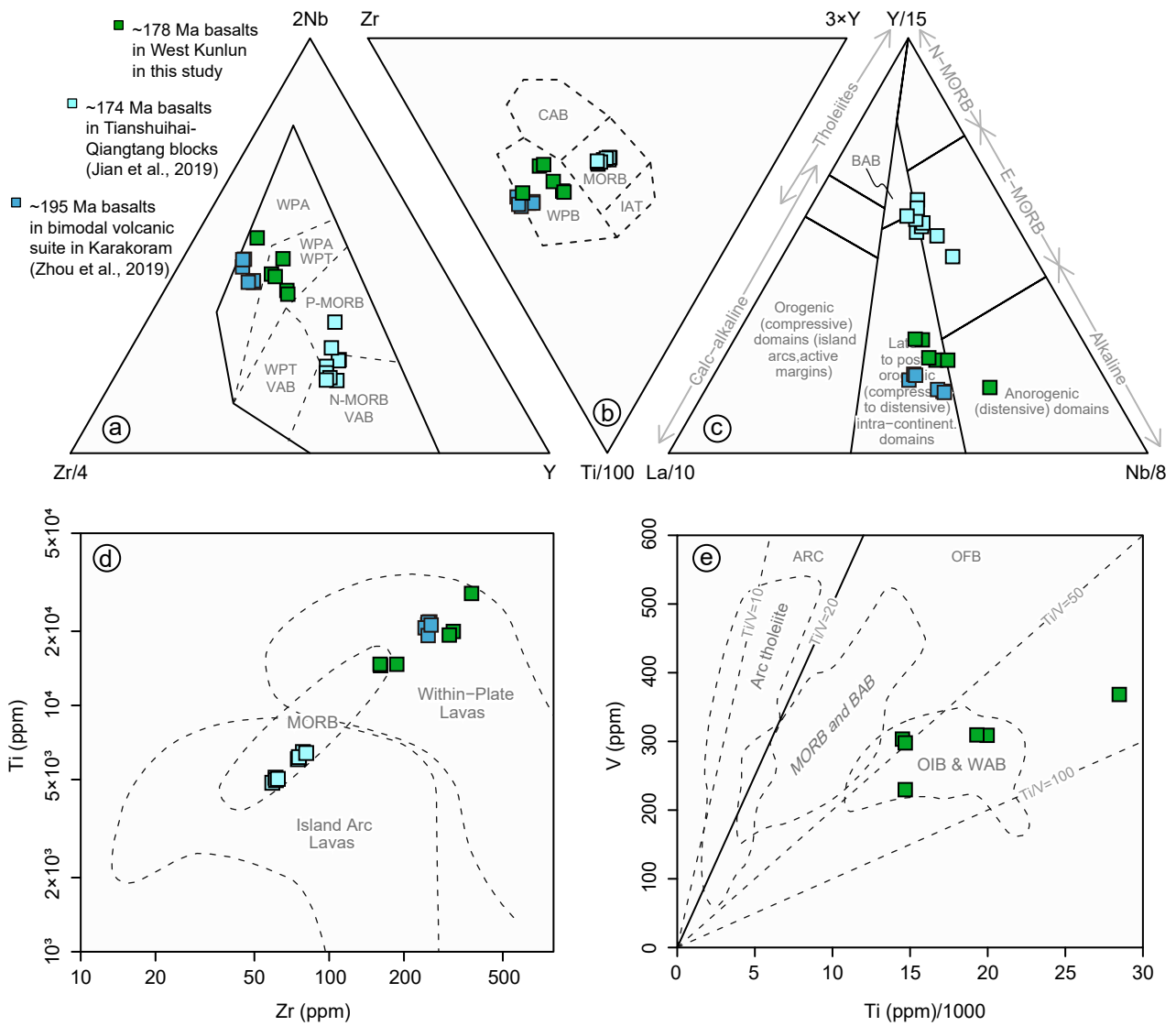


Figure 8 Tectonic discrimination diagrams for Jurassic basalts through (a) Zr/4-2Nb-Y plot and (b) Zr-3Y-Ti/100 plot (Meschede, 1986), (c) La/10-Y/15-Nb/8 plot (Cabani and Lecolle, 1989), (d) Ti-Zr plot (Pearce, 1982) and (e) V-Ti/1000 plot (Rollinson, 1993). Abbreviation: WPB-within plate basalts; WPA/WAB- within plate alkali basalts; WPT-within plate tholeiites; VAB- volcanic arc basalts; CAB- calc-alkali basalts; IAT-island arc tholeiites; BAB-back arc basalts; OIB-ocean island basalts; .

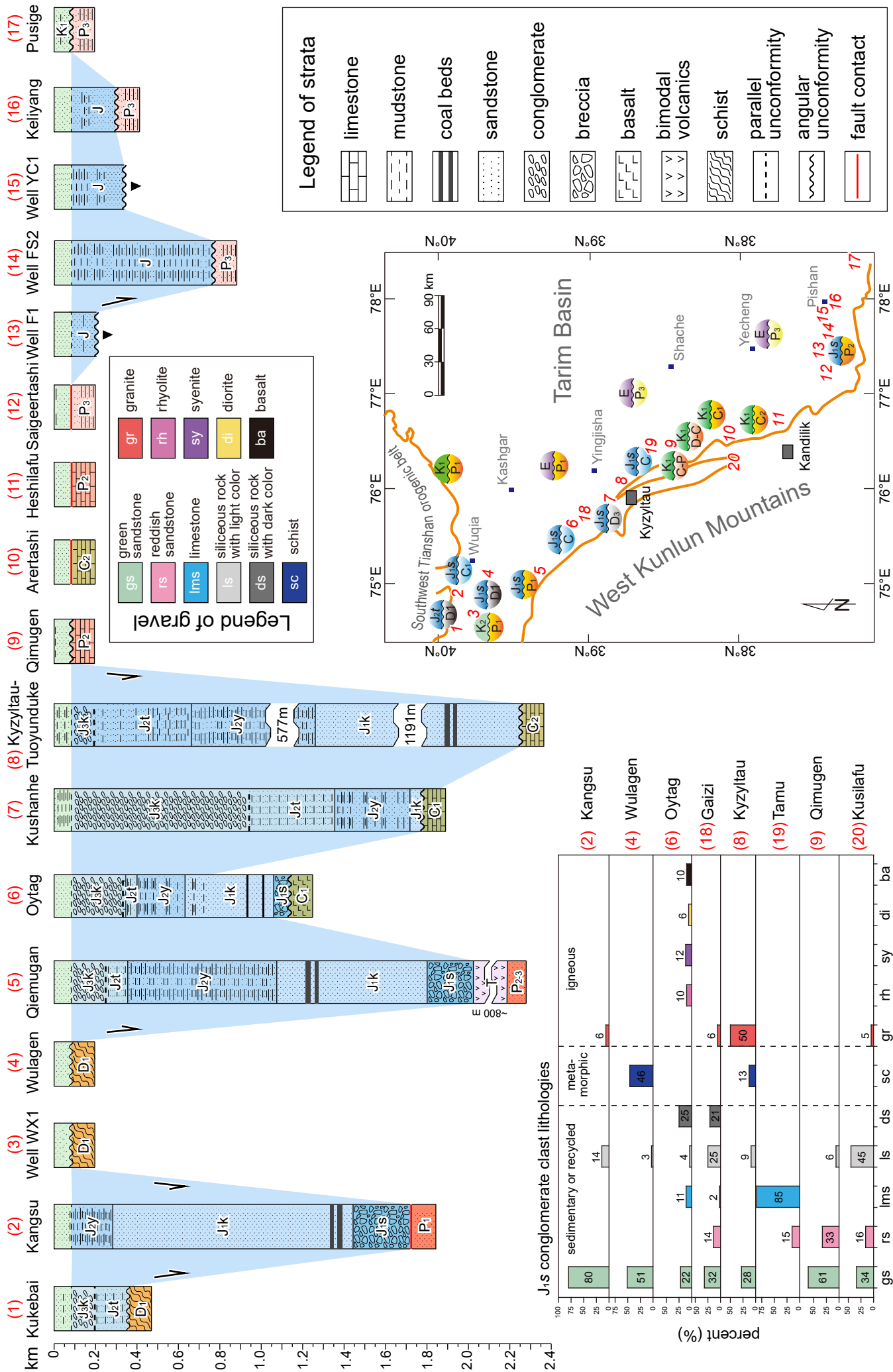


Figure 9 Stratigraphic correlations of Jurassic basin along east flank of the Western Kunlun Mountains (modified from Wu et al., 2021 and Rembe et al., 2022) and the results of gravel analysis of Early Jurassic conglomerate.

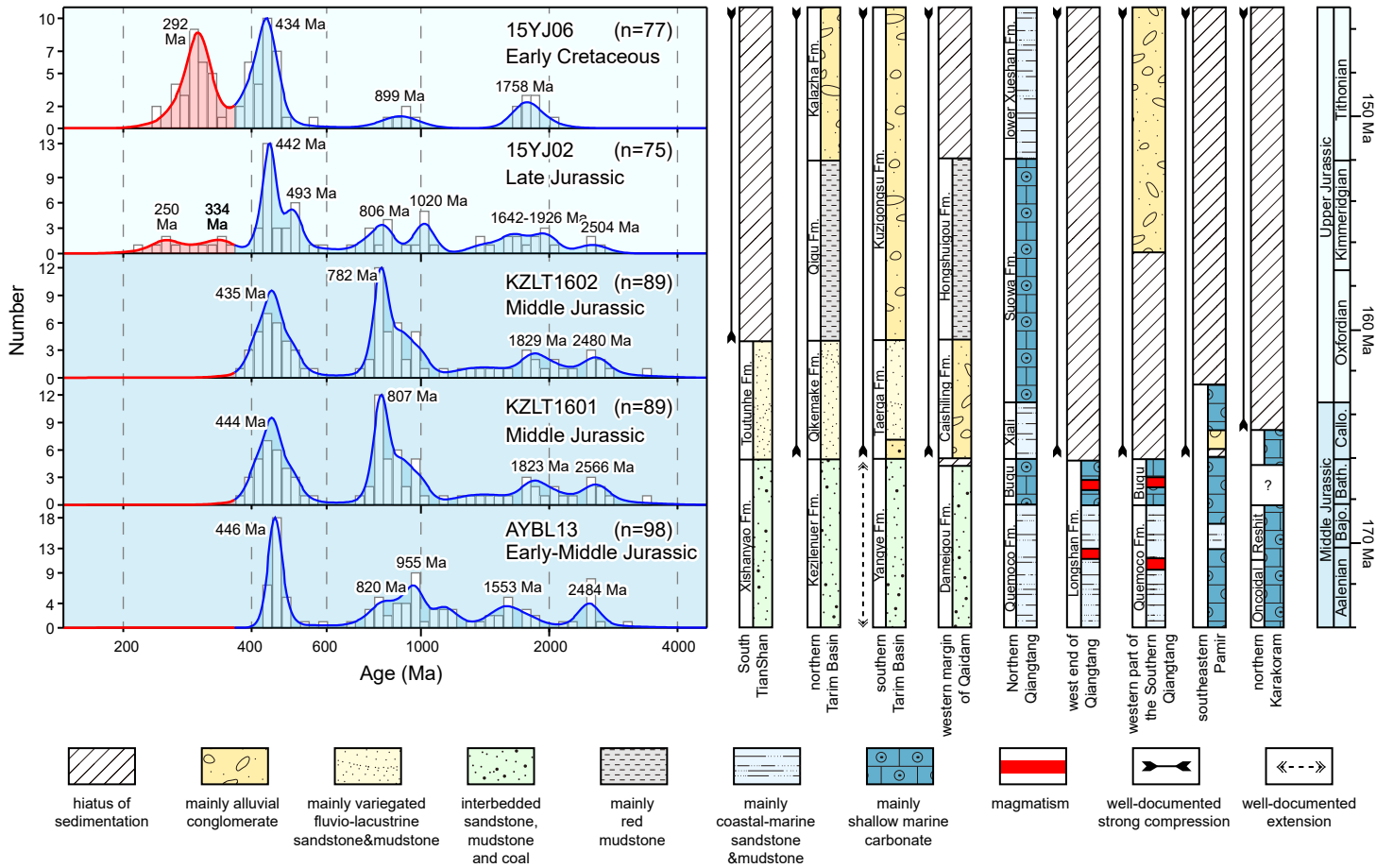


Figure 10 Late Jurassic basin inversion based on the provenance variation through the Early Jurassic to Early Cretaceous and the stratigraphic correlation in the northwestern China. Late Jurassic and Early Cretaceous sandstone samples are according to Zhang et al. (2019b). The sampling locations are shown in Fig. 2a. Stratigraphic correlation is modified from Yang et al. (2017).

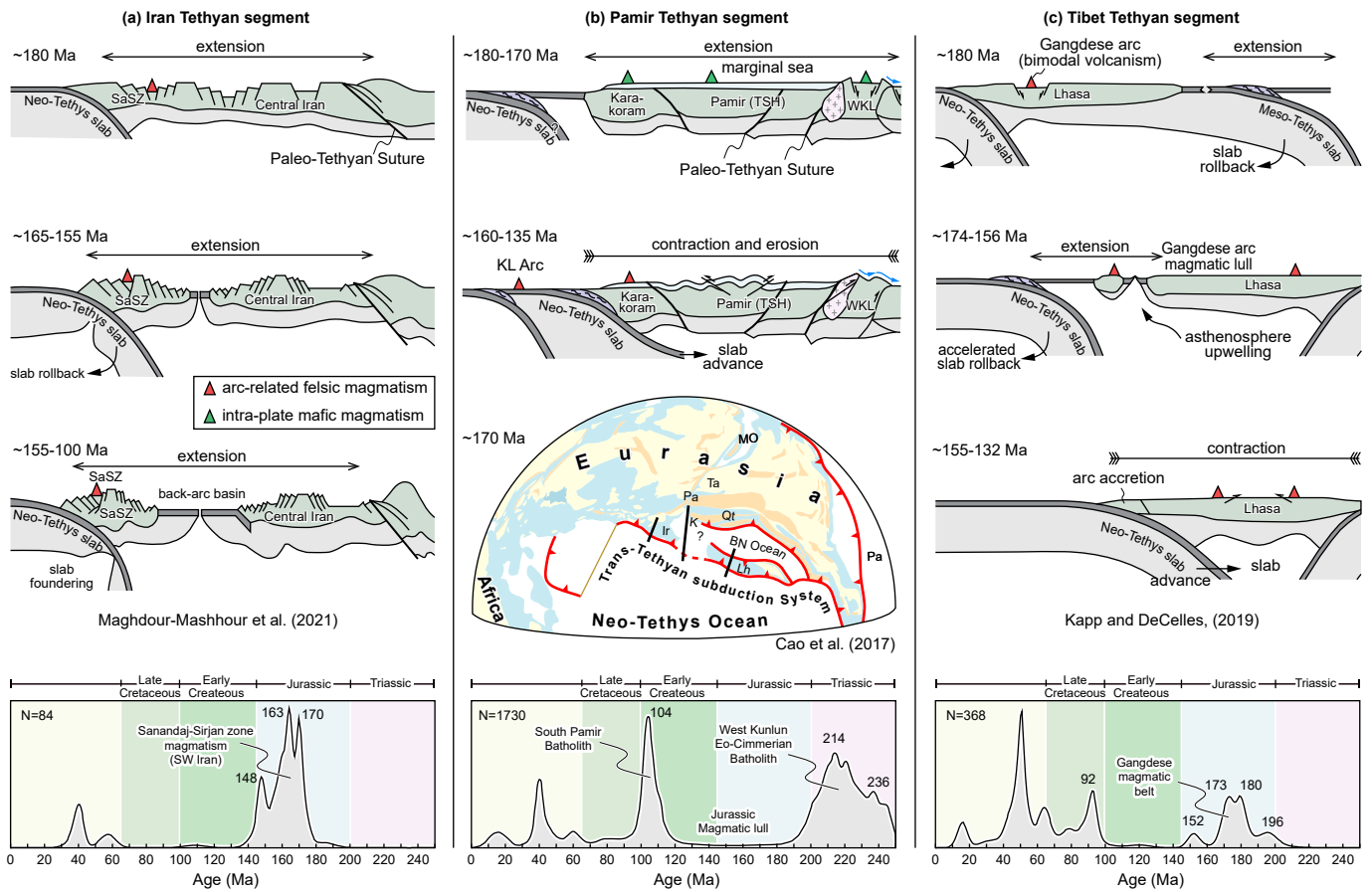


Figure 11 Illustrative cartoons indicating the tectonic variation of the southern Eurasian margin in Jurassic. The subduction of the Neo-Tethys Ocean resulted in persistent rifting along the Iran Tethyan segment, generating massive magmatism during the Early Jurassic to Early Cretaceous. The far-field subduction causing the Early-Middle Jurassic extension along the Pamir Tethyan segment without magmatic flare-up. The changes in subduction style along the Pamir and Tibet Tethyan segments induced the extension-contraction transition. The spatial magmatic datasets are according to Zhang et al. (2018), Chapman et al. (2018), Ma et al. (2017b) and Zhu et al. (2017), and the map of paleogeographic reconstruction is modified from Cao et al. (2017). Abbreviation: SaSZ- Sanandaj-Sirjan zone; TSH-Tianshuihai block; WKL-West Kunkun Mountains; KL Arc- Kohistan Ladakh Arc; Ir-Iran; K- Karakoram; Pa-Pamir; Ta-Tarim; Qt-Qiangtang; Lh-Lhasa; BN Ocean-Bangong-Nujiang Ocean.